A p value of less than 0.05 was taken to indicate a significant difference.

Results

Image acquisition was successfully conducted in all volunteers. The time required for image analysis was approximately 40 minutes per subject. The means and SDs of the SNRs and CNRs are shown in Table 1. Both were highest in group B. Signals of the liver parenchyma, hepatic arteries, and hepatic veins were adequately suppressed. In addition, high inflowing signals into the intrahepatic portal vein were obtained and peripheral portal venous branches were well visualized (Fig. 1). Statistically significant differences were also seen in SNR_{RPV}, $CNR_{RPV\text{-}liver}$, and $CNR_{LPV\text{-}liver}$ (contrast-to-noise ratio of the RPV and LPV compared with the liver parenchyma, respectively) between different groups (Table 1).

The results of qualitative analyses are shown in Table 2. Both the mean visualization scores of vessels and overall image quality were best in group B due to good visualization of the peripheral portal veins and sufficient signal suppression of the liver parenchyma and other vessels. There were significant differences between groups A and D ($p < 0.05$) and groups B and D ($p < 0.01$) in the visualization scores of the RPV. The visualization scores of the peripheral portal branches, such as P4 and P8, were better for groups B and C than the other groups; however, there was no statistically significant difference. Overall image quality was mainly influenced by overlapping signals of other vessels. Overall image quality was significantly worse for group D than for the other groups ($p < 0.01$) because of overlapping of other vessels, especially the

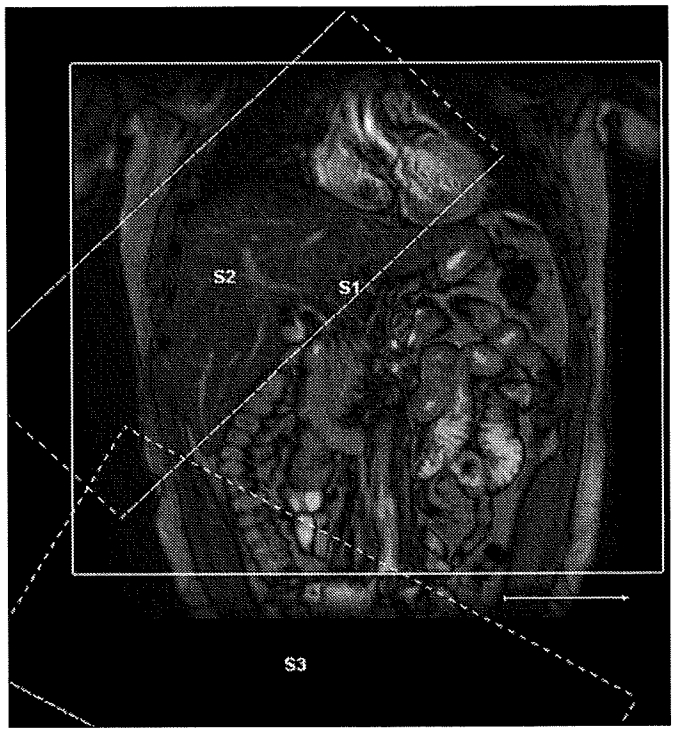

A

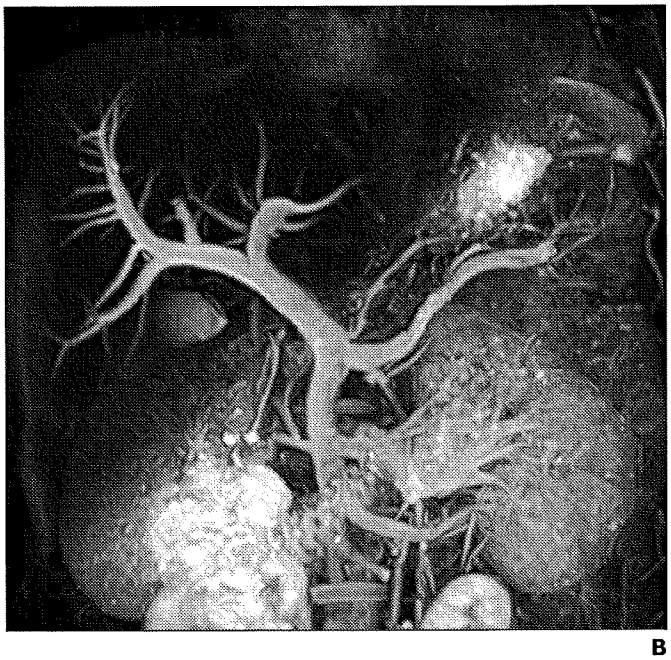

B

C

Fig. 1—Placement of two different oblique time–space labeling inversion pulses (T-SLIPs) for selective visualization of intrahepatic portal venous system.
A, On scout image of healthy 43-year-old male volunteer, one T-SLIP was placed on liver and thorax (S2) and other T-SLIP, on lower abdomen (S3). Rectangular area shows imaging volume (S1).
B and **C,** Coronal maximum-intensity-projection image (**B**) and source image (**C**) of 43-year-old male volunteer in group B (TIs of 1,200 and 1,100 milliseconds) show that portal venous system is selectively visualized in detail without exogenous contrast agent.

TABLE 1: Signal-to-Noise Ratio (SNR) and Contrast-to-Noise Ratio (CNR) Values in Each Group

Value	Group A	Group B	Group C	Group D
SNR_{RPV}	51.5 ± 18.6[a]	55.3 ± 24.5[b]	41.6 ± 19.4	34.8 ± 17.8
SNR_{LPV}	34.7 ± 10.6	43.6 ± 20.2	35.6 ± 15.4	31.6 ± 16.2
$CNR_{RPV\text{-}liver}$	41.2 ± 15.3[b]	44.7 ± 19.4[b,c]	32.1 ± 14.4	25.9 ± 13.1
$CNR_{LPV\text{-}liver}$	24.3 ± 9.8	32.9 ± 16.0[a]	26.1 ± 10.7	22.7 ± 11.5

Note—Data are means ± SD. RPV = right portal vein, LPV = left portal vein. $CNR_{RPV\text{-}liver}$ and $CNR_{LPV\text{-}liver}$ = contrast-to-noise ratio of the RPV and LPV compared with the liver parenchyma, respectively.
[a]Significantly better than group D ($p < 0.05$).
[b]Significantly better than group D ($p < 0.01$).
[c]Significantly better than group C ($p < 0.05$).

TABLE 2: Mean Visualization Scores and Overall Image Quality of Vessels in Each Group

Vessel	Group A	Group B	Group C	Group D
RPV	3.9 ± 0.3[a]	4.0[b]	3.8 ± 0.1	3.6 ± 0.6
LPV	3.6 ± 0.7	3.9 ± 0.2	3.8 ± 0.4	3.6 ± 0.6
P4	3.0 ± 1.0	3.7 ± 0.7	3.7 ± 0.6	3.1 ± 0.8
P8	3.5 ± 0.9	3.9 ± 0.3	3.8 ± 0.4	3.5 ± 0.7
Overall image quality	2.7 ± 0.4[b]	2.9 ± 0.3[b,c]	2.6 ± 0.5[b]	2.0 ± 0.5

Note—Data are means ± SD. Visualization of the LPV, P4, and P8 of groups B and C was better than groups A and D without significant statistical difference. RPV = right portal vein, LPV = left portal vein, P4 = peripheral branch in segment IV, P8 = peripheral branch in segment VIII.
[a]Significantly better than group D ($p < 0.05$).
[b]Significantly better than group D ($p < 0.01$).
[c]Significantly better than group C ($p < 0.05$).

hepatic vein; in addition, image quality of group B was significantly better than that of group C ($p < 0.05$).

The differences in image quality among the groups are presented in Figure 2. In group A, the TI of 800 milliseconds was not enough for inflowing portal flow to reach the periphery. On the other hand, the TI of 2,000 milliseconds in group D allowed signal recovery of the liver parenchyma and hepatic veins, and the peripheral portal venous signal sometimes became unclear in MIP images. Intrahepatic portal venous anatomy was well visualized in all subjects (Fig. 3). There were three cases of right anterior branch arising from the LPV.

Discussion

A detailed map of the portal venous anatomy is an important tool for surgeons to plan hepatic resection and living related donor liver transplantation [14–16]. In the past, conventional angiography was the standard method for visualization of the portal venous anatomy. More recently, MDCT has been playing one of the most important roles in the assessment of liver anatomy owing to its easy accessibility and its shorter examination time. This might reduce the need for multitechnique evaluation protocols [17]. However, the necessity of administering considerable volumes of potentially nephrotoxic iodinated contrast agents and of exposure to ionizing radiation are considerable disadvantages of the CT protocol.

On the other hand, MRA has been established as a valuable technique in detecting vascular disease without radiation exposure. In previous studies, 3D contrast-enhanced MR portography has been shown to be as effective as digital subtraction angiography for assessing the portal vein [18, 19]. Although MR contrast agents were thought to be much safer than CT contrast media, a serious adverse reaction called nephrogenic systemic fibrosis has recently been reported to occur after exposure to gadolinium-based contrast agents [20]. Hence, selective visualization of the portal vein with unenhanced MRA would be beneficial for the patient.

Half-Fourier FSE is one of the new unenhanced MRA techniques [21]. It allows coronal acquisition, which is not possible with time-of-flight imaging, especially for body MRA, and thus enables shorter 3D acquisition time [22, 23]. In addition, this sequence is T2-weighted and the liver parenchyma becomes relatively low signal intensity, resulting in good contrast between the portal vein and liver parenchyma; however, the long TE decreases the signal at the portal confluence where higher flow velocity might cause flow void in comparison with images acquired with true SSFP [1]. Also, selective visualization of the portal vein by this technique alone is not feasible.

Application of T-SLIPs in this study resulted in good signal suppression of the liver parenchyma and the vessels of no interest, which allowed selective visualization of the intrahepatic portal venous system without the use of contrast medium. When quantitative and qualitative analyses are summarized, the images of group B (TIs = 1,200 and 1,100 milliseconds) were the best and were optimal because the T-SLIP with those TIs attained both signal suppression of the liver parenchyma and vessels of no interest and inflow of portal venous signal to the periphery. The mean portal venous peak velocity has been reported to be 19.5 cm/s [24], so a TI of 1,200 milliseconds was considered sufficient for peripheral portal venous visualization. In group A, the TI of 800 milliseconds was not enough for inflowing portal flow to reach the periphery, so the visualization score of the peripheral branches (P4 and P8) was lower than in group B. On the other hand, the TI of 2,000 milliseconds in group D induced signal recovery of the liver parenchyma and hepatic veins and led to deterioration of the CNR.

Other structures that overlapped with the portal vein were the IVC and the biliary tract. Complete suppression of the IVC was not attained in all subjects because the T-SLIP on the lower abdomen did not cover the entire area of the IVC. The T-SLIP was placed to suppress the IVC signal, but at the same time, it was required to minimize suppression of blood signals in the superior and inferior mesenteric veins that flow into the portal vein. The ambivalence had resulted in incomplete suppression of the IVC in some subjects. Also biliary tracts sometimes overlapped with the portal vein in MIP images; however, by using source images in combination with MIP images, it did not cause a substantial problem to evaluate the intrahepatic portal vein.

Compared with contrast-enhanced MRA, our technique has several advantages. In general, high contrast between the portal vein and surrounding tissue is difficult to attain using contrast material because signals of

the liver parenchyma have already been high in the portal venous phase [2, 25]. In addition, to obtain high-level contrast between the vessels and surrounding tissue using contrast-enhanced MRA, data acquisition must be performed within a brief acquisition window during the first pass of the contrast agent [26]. Hence, optimal bolus timing is crucial and all data must be acquired during a single breath-hold, which limits spatial resolution [27]. On the contrary, there is no time constraint in our approach and it facilitates data acquisition for increased spatial resolution even in patients with a reduced breath-hold capability due to the use of respiratory-gating technology. Additionally, our approach dispels concerns about the adverse effects of contrast agents such as anaphylactic shock.

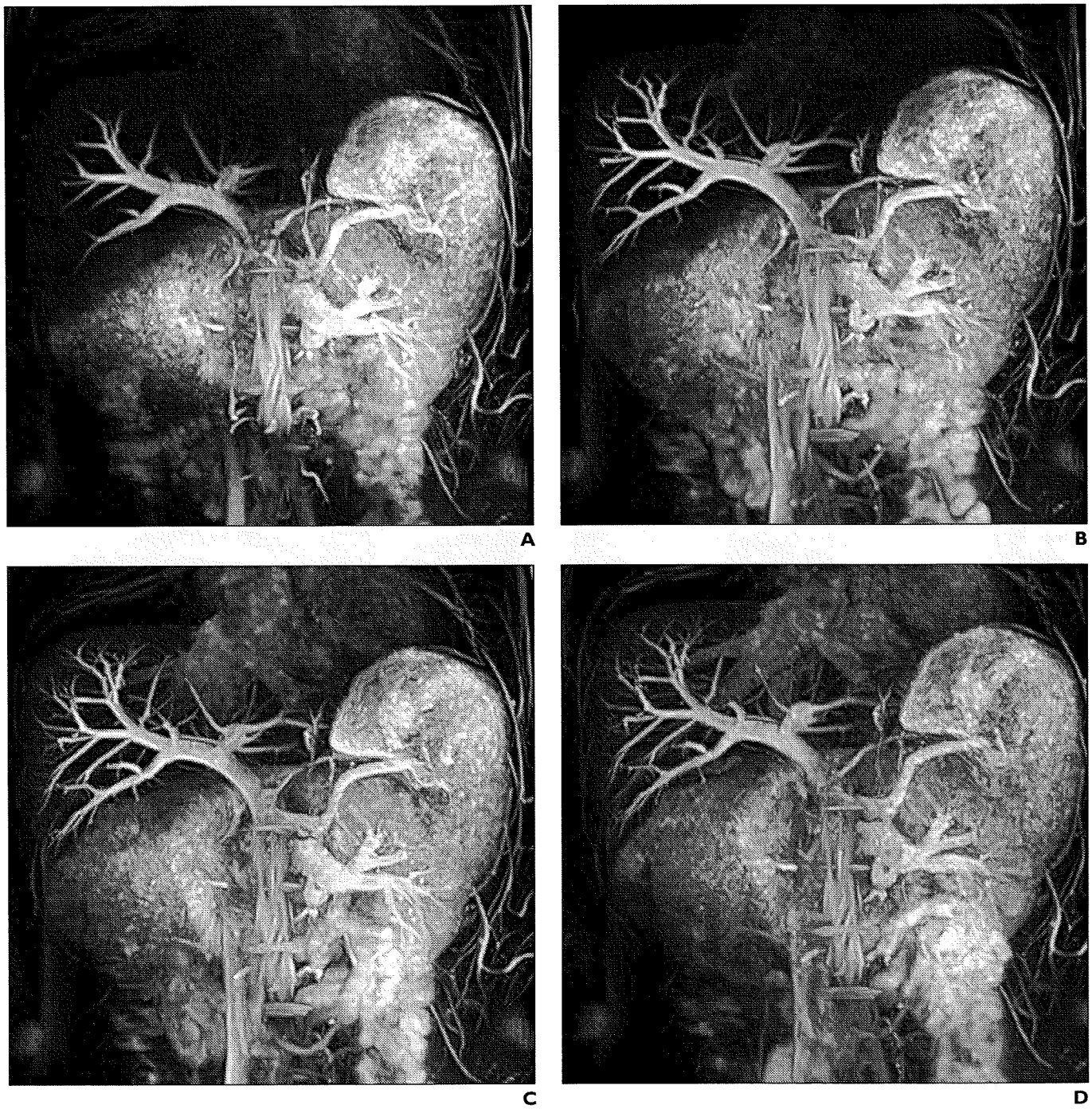

Fig. 2—Image quality differs depending on inversion time (TI).
A–D, Coronal maximum-intensity-projection images of healthy 40-year-old male volunteer illustrate changes between groups with different TIs: group A (**A**), 800 and 1,100 milliseconds; group B (**B**), 1,200 and 1,100 milliseconds; group C (**C**), 1,600 and 1,100 milliseconds; and group D (**D**), 2,000 and 1,100 milliseconds. Gradual portal venous inflow into periphery and signal recovery of liver parenchyma and hepatic veins were observed concurrently when TI was increased.

A

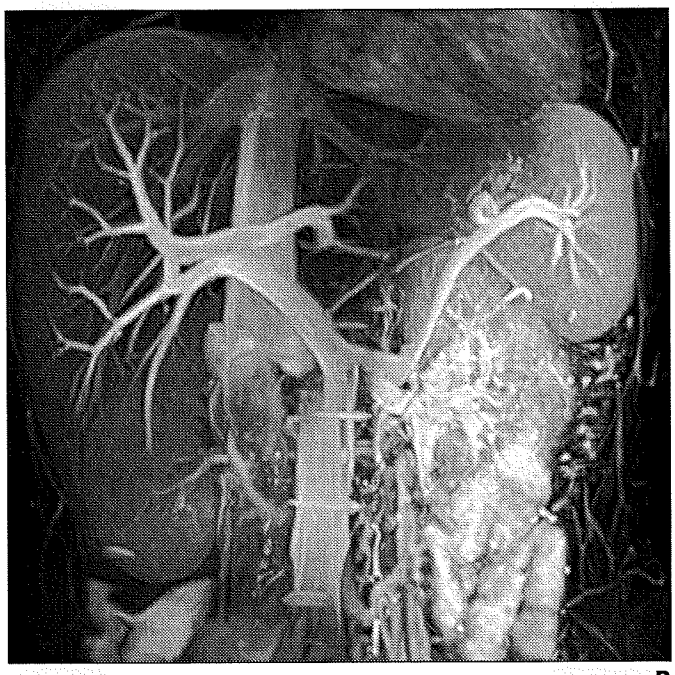

B

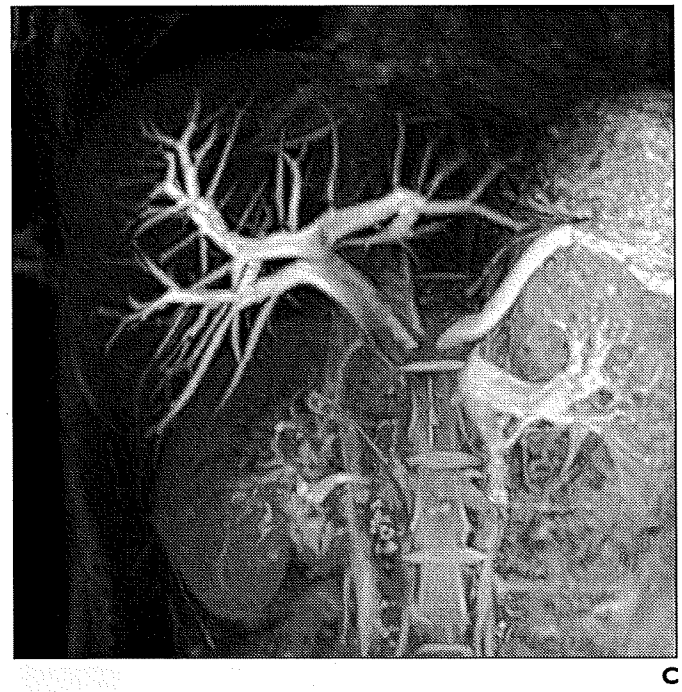

C

Fig. 3—Normal anatomy and anatomic variations of portal vein were visualized.
A, Coronal maximum-intensity-projection (MIP) image of healthy 28-year-old male volunteer in group B (TIs, 1,200 and 1,100 milliseconds) shows normal portal bifurcation. Peripheral portal venous branches are also well seen.
B and **C,** Coronal MIP images of healthy 23-year-old female volunteer in group C (**B**) (TIs, 1,600 and 1,100 milliseconds) and healthy 27-year-old male volunteer in group B (**C**) (TIs, 1,200 and 1,100 milliseconds). Both images show normal variation of portal vein that right posterior branch diverges directly from main trunk and right anterior branch arises from left portal vein.

Patients with severe renal impairment can undergo this examination.

Our study had several limitations. The main limitation was the absence of a reference standard with which to compare the results of our qualitative analysis. Hepatic angiography or surgical exploration would have provided a more definitive determination of the portal venous anatomy in each subject, but this study aimed at optimization of the scanning parameters, and a comparative study with a reference standard is our next aim. Another limitation is that only healthy adult subjects were examined. The proposed method is dependent on inflow of portal signal, but it is reduced or even reversed in some patients with portal hypertension [28]. In addition, visualization of the distal portal branches might be impaired, and longer TIs, such as 1,600 milliseconds, would be better than 1,200 milliseconds despite the decrease in CNR by signal recovery of the liver parenchyma. Further studies will involve a larger sample size and include patients with conditions requiring visualization of the portal venous anatomy.

In conclusion, the combination of a respiratory-triggered 3D half-Fourier FSE sequence and T-SLIPs enabled selective visualization of the intrahepatic portal vein during

free breathing without an exogenous contrast agent. High contrast visualization was obtained while signals from other vessels and the liver parenchyma were adequately suppressed. Our preliminary data suggest that this technical approach has clinical promise.

Acknowledgments

We thank Nobuyasu Ichinose, Ayako Ninomiya, and Saori Satou (Toshiba Medical Systems Corporation) for their excellent technical assistance and advice on sequence optimization.

References

1. Smith CS, Sheehy N, McEniff N, Keogan MT. Magnetic resonance portal venography: use of fast-acquisition true FISP imaging in the detection of portal vein thrombosis. *Clin Radiol* 2007; 62:1180–1188
2. Lee MW, Lee JM, Lee JY, et al. Preoperative evaluation of hepatic arterial and portal venous anatomy using the time resolved echo-shared MR angiographic technique in living liver donors. *Eur Radiol* 2007; 17:1074–1080
3. Heilmaier C, Sutter R, Lutz AM, et al. Mapping of hepatic vascular anatomy: dynamic contrast-enhanced parallel MR imaging compared with 64 detector row CT. *Radiology* 2007; 245:872–880
4. Buhaescu I, Izzedine H. Gadolinium-induced nephrotoxicity. *Int J Clin Pract* 2008; 62:1113–1118
5. Katoh M, Spuentrup E, Stuber M, et al. Free-breathing renal magnetic resonance angiography with steady-state free-precession and slab-selective spin inversion combined with radial k-space sampling and water-selective excitation. *Magn Reson Med* 2005; 53:1228–1233
6. Miyazaki M, Takai H, Sugiura S, et al. Peripheral MR angiography: separation of arteries from veins with flow-spoiled gradient pulses in electrocardiography-triggered three-dimensional half-Fourier fast spin-echo imaging. *Radiology* 2003; 227:890–896
7. Weber OM, Martin AJ, Higgins CB. Whole-heart steady-state free precession coronary artery magnetic resonance angiography. *Magn Reson Med* 2003; 50:1223–1228
8. Shimada K, Isoda H, Okada T, et al. Non-contrast-enhanced hepatic MR angiography with true steady-state free-precession and time spatial labeling inversion pulse: optimization of the technique and preliminary results. *Eur J Radiol* 2008 Feb 2 [Epub ahead of print]
9. Ito K, Koike S, Jo C, et al. Intraportal venous flow distribution: evaluation with single breath-hold ECG-triggered three-dimensional half-Fourier fast spin-echo MR imaging and a selective inversion-recovery tagging pulse. *AJR* 2002; 178: 343–348
10. Constable RT, Gore JC. The loss of small objects in variable TE imaging: implications for FSE, RARE, and EPI. *Magn Reson Med* 1992; 28:9–24
11. Garcia DM, Duhamel G, Alsop DC. Efficiency of inversion pulses for background suppressed arterial spin labeling. *Magn Reson Med* 2005; 54: 366–372
12. Bernstein MA, King FK, Zhou XJ. *Handbook of MRI pulse sequences*. London, UK: Elsevier Academic Press, 2004:960–962
13. Isoda H, Kataoka M, Maetani Y, et al. MRCP imaging at 3.0 T vs. 1.5 T: preliminary experience in healthy volunteers. *J Magn Reson Imaging* 2007; 25:1000–1006
14. Curley SA, Chase JL, Roh MS, Hohn DC. Technical considerations and complications associated with the placement of 180 implantable arterial infusion devices. *Surgery* 1993; 114:928–935
15. Guiney MJ, Kruskal JB, Sosna J, et al. Multi-detector row CT vascular anatomy of the surgical plane in split-liver transplantation. *Radiology* 2003; 229:401–407
16. Kapoor V, Brancatelli G, Federle MP, Katyal S, Marsh JW, Geller DA. Multidetector CT arteriography with volumetric three-dimensional rendering to evaluate patients with metastatic colorectal disease for placement of a floxuridine infusion pump. *AJR* 2003; 181:455–463
17. Schroeder T, Malago M, Debatin JF, et al. "All-in-one" imaging protocols for the evaluation of potential living liver donors: comparison of magnetic resonance imaging and multidetector computed tomography. *Liver Transpl* 2005; 11:776–787
18. Kreft B, Strunk H, Flacke S, et al. Detection of thrombosis in the portal venous system: comparison of contrast-enhanced MR angiography with intraarterial digital subtraction angiography. *Radiology* 2000; 216:86–92
19. Ito K, Blasbalg R, Hussain SM, Mitchell DG. Portal vein and its tributaries: evaluation with thin-section three-dimensional contrast-enhanced dynamic fat-suppressed MR imaging. *Radiology* 2000; 215:381–386
20. Marckmann P, Skov L, Rossen K, et al. Nephrogenic systemic fibrosis: suspected etiological role of gadodiamide used for contrast-enhanced magnetic resonance imaging. *J Am Soc Nephrol* 2006; 17:2359–2362
21. Miyazaki M, Lee VS. Nonenhanced MR angiography. *Radiology* 2008; 248:20–43
22. Miyazaki M, Sugiura S, Tateishi F, Wada H, Kassai Y, Abe H. Non-contrast-enhanced MR angiography using 3D ECG-synchronized half-Fourier fast spin echo. *J Magn Reson Imaging* 2000; 12:776–783
23. Miyazaki M, Ichinose N, Sugiura S, et al. A novel MR angiography technique: swap phase encode extended data (SPEED) acquisition using half-Fourier RARE. *J Magn Reson Imaging* 1998; 8:505–507
24. Sugimoto H, Kaneko T, Hirota M, Inoue S, Takeda S, Nakao A. Physical hemodynamic interaction between portal venous and hepatic arterial blood flow in humans. *Liver Int* 2005; 25: 282–287
25. Lim JS, Kim MJ, Kim JH, et al. Preoperative MRI of potential living-donor-related liver transplantation using a single dose of gadobenate dimeglumine. *AJR* 2005; 185:424–431
26. Grist TM. Magnetic resonance angiography of renal arterial stenosis. *Coron Artery Dis* 1999; 10:151–156
27. Maki JH, Chenevert TL, Prince MR. Contrast-enhanced MR angiography. *Abdom Imaging* 1998; 23:469–484
28. Gaiani S, Bolondi L, Li Bassi S, Zironi G, Siringo S, Barbara L. Prevalence of spontaneous hepatofugal portal flow in liver cirrhosis: clinical and endoscopic correlation in 228 patients. *Gastroenterology* 1991; 100:160–167

Spin-echo T1-weighted Imaging of the Brain with Interleaved Acquisition and Presaturation Pulse at 3 T:

A Feasibility Study Before Clinical Use[1]

Seiko Kasahara, MD, Yukio Miki, MD, PhD, Nobuyuki Mori, MD, Shin-ichi Urayama, PhD, Mitsunori Kanagaki, MD, PhD, Yasutaka Fushimi, MD, PhD, Chikara Maeda, MD, Nobukatsu Sawamoto, MD, PhD, Hidenao Fukuyama, MD, PhD, Kaori Togashi, MD, PhD

Rationale and Objectives. Although spin-echo (SE) sequence has some advantages over gradient-echo sequence in brain imaging, gradient-echo sequence is commonly used for T1-weighted imaging (T1WI) at 3 T because contrast on SE T1WI is widely believed to be poor at 3 T. Recently, gray-white matter contrast on single-slice and multi-slice SE imaging with interslice gap was reported as better at 3 T than at 1.5 T. This study examined the feasibility of interleaved SE T1WI of the brain at 3 T. This study also examined whether presaturation pulse (PP) sufficiently suppresses intra-arterial signals because these signals tend to be hyperintense due to longer T1 at 3 T.

Materials and Methods. Subjects consisted of 18 healthy volunteers. Two sets of T1WI were performed using SE sequence. One set consisted of imaging without PP, and the other consisted of imaging with PP. Each set contained three types of gapless imaging as follows; sequential, 100% interleaved, and 200% interleaved imaging. In each subject, contrast-to-noise ratio between gray-matter and white-matter ($CNR_{GM\text{-}WM}$) and intra-arterial signals were evaluated.

Results. $CNR_{GM\text{-}WM}$ was significantly higher on interleaved images than on sequential images, regardless of PP ($P < .0001$). PP sufficiently suppressed intra-arterial signals ($P < .0001$).

Conclusion. $CNR_{GM\text{-}WM}$ on SE T1WI at 3 T can be improved by interleaved acquisition, and PP sufficiently suppressed intra-arterial signals. Interleaved SE T1WI with PP appears clinically feasible at 3 T.

Key Words. Spin-echo sequence; T1-weighted image; brain; 3 T.

Gradient-echo (GRE) magnetic resonance (MR) sequences, such as magnetization-prepared rapid acquisition gradient echo and spoiled gradient echo, are commonly used for T1-weighted imaging at 3 T (1,2), since the contrast between gray matter (GM) and white matter (WM) on spin-echo (SE) T1-weighted imaging is widely believed to be lower at 3 T than at 1.5 T (2–5). On the other hand, some reports assessed a better contrast-to-noise ratio at 3 T by using optimized parameters on SE T1-weighted sequence (6,7).

SE sequence has several advantages in use for T1-weighted imaging. One is that magnetic susceptibility artifacts are less prominent on SE sequence than on GRE sequence (8). Another advantage of SE sequence is that patent intra-arterial lumens appear hypointense ("flow-void") on SE images, which enable differentiation between patent lumens and subacute intraluminal clots. On the other hand, GRE sequence appears not only intra-arterial subacute clots but also patent intra-arterial lumens as hyperintensity, so

Acad Radiol 2009; 16:852–857

[1] From the Department of Diagnostic Imaging and Nuclear Medicine (S.K., Y.M., N.M., M.K., C.M., K.T.) and Human Brain Research Center (S.U., N.S., H.F.), Graduate School of Medicine, Kyoto University, 54 Shogoin-Kawaharacho, Sakyo-ku, Kyoto 606-8507, Japan; and Department of Radiology, Hikone Municipal Hospital, Shiga, Japan (Y.F.). Received October 17, 2008; accepted December 30, 2008. **Address correspondence to:** Y.M. e-mail: mikiy@kuhp.kyoto-u.ac.jp

doi:10.1016/j.acra.2008.12.026

intra-arterial subacute clots could be easily missed on GRE (9). GRE imaging alone should not be used to determine the patency of aneurysms or cerebral arteriovenous malformations in the absence of corroborative images, particularly SE sequence (9). We recently demonstrated that contrast between GM and WM on single-slice SE T1-weighted MR images is better at 3 T than at 1.5 T (10). Moreover, we revealed that the influence of multi-slice imaging on contrast between GM and WM is significantly higher at 3 T than at 1.5 T, and suggested that SE T1-weighted imaging may be applicable at 3 T with sufficient interslice gap.

The present study examined differences in GM-WM contrast between sequential and interleaved SE T1-weighted imaging. Additionally, presaturation pulse (PP) was applied to suppress intra-arterial lumens (11), since intra-arterial lumens on T1-weighted imaging may tend to be hyperintense by paradoxical enhancement due to longer T1 relaxation time at 3 T. The present study also examined whether PP can sufficiently suppress intra-arterial signals. We therefore aimed to show that interleaved SE sequence with PP is feasible for acquisition of T1-weighted images of the brain with sufficient GM-WM contrast and sufficient suppression of intra-arterial signals.

MATERIALS AND METHODS

Subjects

Subjects comprised 18 volunteers (10 men, 8 women; mean age, 29 years; range, 24–38 years). All subjects were neurologically examined by a neurologist (N.S.) and were considered neurologically healthy. Each subject provided written informed consent.

Imaging Protocols

Whole brain scanning was performed using a 3 T MR scanner (Magnetom Trio; Siemens, Erlangen, Germany) using an 8-channel head coil. The head of the subject was fixed by means of a foam pad within the head coil, and subjects were instructed not to move during MR acquisition.

T1-weighted imaging was performed using SE sequence with: repetition time (TR), 600 ms; echo time (TE), 7.5 ms; slice thickness, 5 mm; number of averages, 1; number of slices, 24; matrix size, 256 × 256; flip angle, 90°; bandwidth, 190 Hz. One acquisition scheme consisted of images without PP, and the other consisted of images with PP; 50 mm-thick PP band was applied 10 mm below the imaging field. Each acquisition scheme contained three types of gapless images: sequential, 100% interleaved, and 200% interleaved imaging (Fig 1). Scan times were as follows: total sampling times were 158 s for sequential image, 314 s for 100% interleaved images (one interleaved acquisition sampling time was 157 s), and 450 s for 200% interleaved images (one interleaved acquisition sampling time was 150 s), respectively. Scan times were almost the same between acquisition scheme without PP and with PP at the same type of gapless image. Specific absorption rates of all acquisitions were within Food and Drug Administration guideline limits (12).

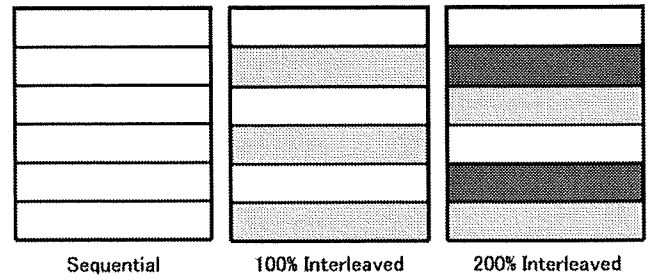

Figure 1. Illustration of acquisition schemes.

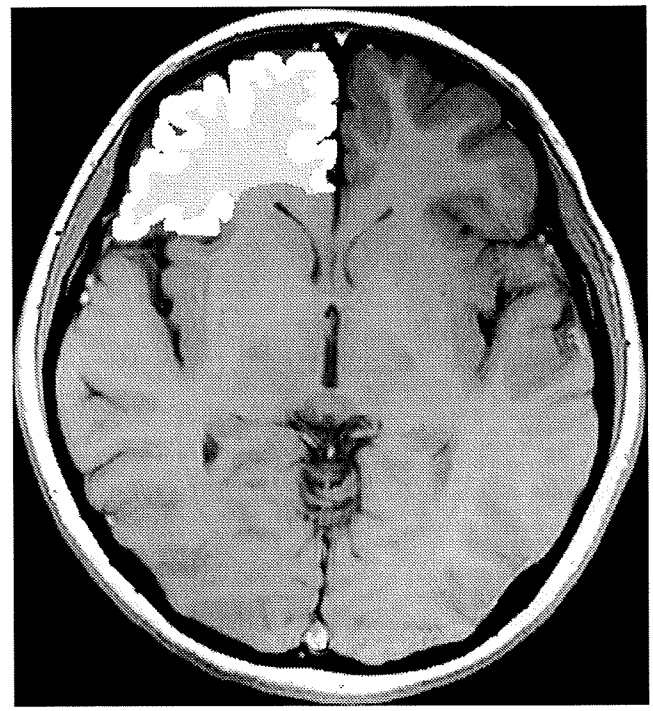

Figure 2. Representative image of a region-of-interest (ROI) on spin-echo T1-weighted imaging. Areas of gray matter and white matter in the frontal lobes were selected as ROIs.

Analysis of Contrast-to-Noise Ratio (CNR)

GM and WM of the right frontal lobe and background were manually selected as regions-of-interest (ROIs) at the level of the basal ganglia (Fig 2), according to a previous study (10). ROIs of the background signal were carefully placed so that ghost artifacts along the phase-encoding direction were not included. In each subject, the same ROIs were evaluated and CNR between GM and WM (CNR_{GM-WM}) was calculated as the difference between signal intensities (SI) of GM and WM

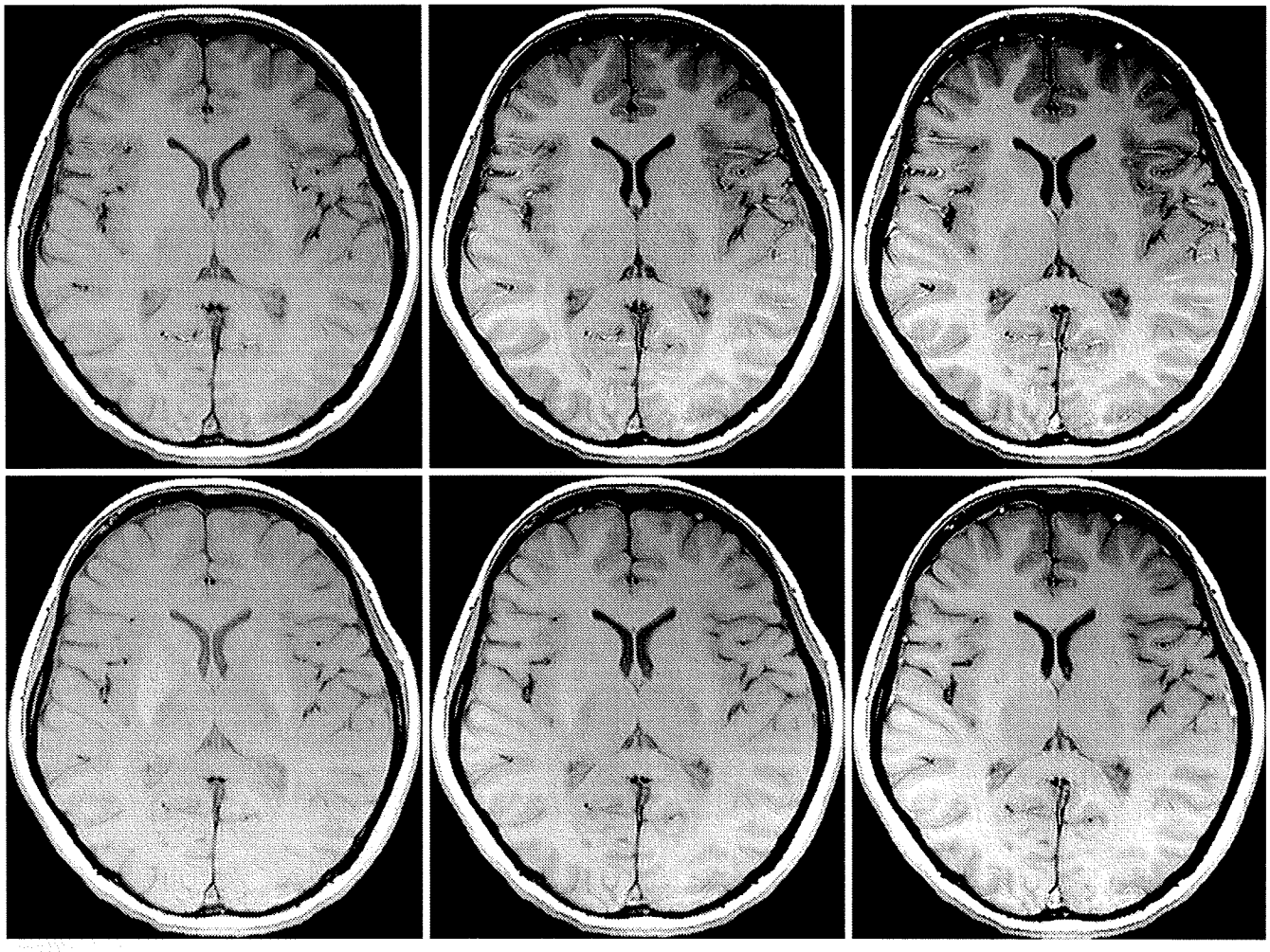

Figure 3. Spin-echo T1-weighted gapless multi-slice imaging without presaturation pulse (PP) (*upper row*) and with PP (*lower row*) at the level of the basal ganglia. From left to right, sequential imaging, 100% interleaved imaging, and 200% interleaved imaging are displayed. Gray matter and white matter contrast was more conspicuous with either 100% or 200% interleaved imaging than with sequential imaging.

divided by the standard deviation (SD) of the background: $| SI_{GM} - SI_{WM} | / SD_{background}$ (10). ROIs were drawn using ImageJ ver. 1.37 software (National Institutes of Health, Bethesda, MD).

Differences in $CNR_{GM\text{-}WM}$ among sequential images, 100% interleaved images, and 200% interleaved images were statistically analyzed by one-way repeated-measures analysis of variance for each acquisition scheme. Differences among means were then analyzed using post-hoc Tukey-Kramer multiple comparisons testing. Values of $P < .05$ were considered statistically significant. In addition, $CNR_{GM\text{-}WM}$ differences between acquisition schemes without PP and with PP in each of the three types of images (sequential, 100% interleaved, and 200% interleaved) were analyzed by paired *t*-tests. Values of $P < .05$ were considered statistically significant. Statistical analyses were performed using JMP ver. 5.1 software (SAS Institute, Cary, NC).

Analysis of Intra-arterial Signal

To evaluate the effect of PP on intra-arterial signals, those in the vertebral and basilar arteries were visually assessed by two independent, experienced neuroradiologists. These arteries were selected because they run in a vertical direction to the image plane and because they are frequent sites of dissection. Intra-arterial signals were expressed as: grade 0, no signal; grade 1, mixed signals; and grade 2, entirely hyperintense signal. If discrepancies existed between the two readers, consensus was obtained in discussion after both reading sessions were completed. Differences in grade of intra-arterial signals on the two acquisition schemes with and without PP were statistically assessed with Wilcoxon's

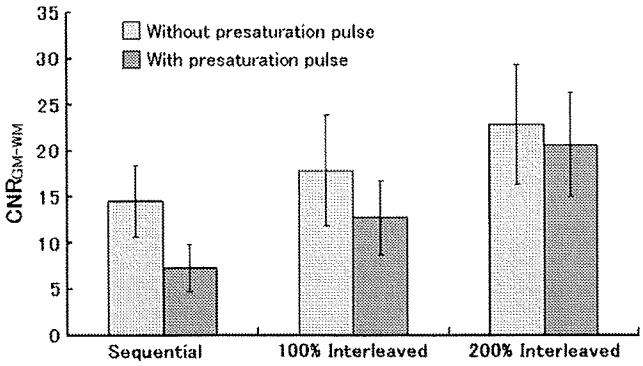

Figure 4. Contrast-to-noise ratio between gray-matter and white-matter (CNR_{GM-WM}) of sequential, 100% interleaved, and 200% interleaved imaging. Light gray, without presaturation pulse (PP); dark gray, with PP. Error bars represent standard deviations. Without PP, CNR_{GM-WM} for sequential, 100% interleaved, and 200% interleaved imaging was 14.48 ± 3.90, 17.85 ± 6.04, and 22.80 ± 6.56, respectively. With PP, CNR_{GM-WM} for sequential, 100% interleaved, and 200% interleaved imaging was 7.21 ± 2.57, 12.70 ± 4.04, and 20.61 ± 5.67, respectively.

signed rank test using JMP ver. 5.1 software. Values of $P < .05$ were considered statistically significant.

Institutional review board approval was obtained for this study.

RESULTS

On acquisition without PP, CNR_{GM-WM} of sequential, 100% interleaved, and 200% interleaved imaging was 14.48 ± 3.90, 17.85 ± 6.04, and 22.80 ± 6.56, respectively, showing significant differences ($P < .0001$). Post-hoc Tukey-Kramer multiple comparisons revealed a significant difference in CNR between sequential imaging and 100% interleaved imaging, and between sequential imaging and 200% interleaved imaging ($P < .01$). On acquisition scheme with PP, CNR_{GM-WM} of sequential, 100% interleaved, and 200% interleaved imaging was 7.21 ± 2.57, 12.70 ± 4.04, and 20.61 ± 5.67, respectively, representing a significant difference ($P < .0001$). Post-hoc Tukey-Kramer multiple comparisons testing revealed a significant difference among all imaging schemes ($P < .01$) (Figs 3 and 4). Application of PP significantly reduced CNR_{GM-WM} for all three imaging schemes ($P < .0001$ for sequential imaging, $P < .0001$ for 100% interleaved imaging, and $P = .0431$ for 200% interleaved imaging). CNR_{GM-WM} reduction rate by the application of PP on sequential, 100% interleaved, and 200% interleaved imaging was 50.21%, 28.85%, and 9.61%, respectively.

The effects of PP on vertebral and basilar intra-arterial signals are summarized in Table 1. On acquisition schemes without PP, vertebral intra-arterial signals were either grade 1 (mixed signals) or grade 2 (entirely hyperintense signal) in 17 volunteers (94%) on all three types of imaging, and basilar intra-arterial signals were shown in grade 1 or grade 2 in 18 volunteers (100%) on sequential imaging, and in 17 volunteers (94%) on 100% interleaved and 200% interleaved imaging. Conversely, on all the three types of imaging with PP, vertebral and basilar intra-arterial signals showed no signal (grade 0). Intra-arterial signals were significantly suppressed with application of PP (Fig 5) ($P < .0001$).

DISCUSSION

This study revealed that interleaved SE T1-weighted imaging produced significantly higher GM-WM contrast than sequential SE T1-weighted imaging at 3 T. In addition, PP satisfactorily suppressed intra-arterial signals on SE T1-weighted imaging at 3 T.

We believe that cross-talk effect is one of the reasons why interleaved SE T1-weighted imaging offers better GM-WM contrast than sequential imaging at 3 T. Cross-talk effect is an important factor in the contrast on SE imaging, which can result in decreased signal and concomitant decreases in contrast (13,14). Cross-talk effect may be stronger in a higher magnetic field because recovery of the excited spin by cross-talk effect is prolonged due to longer T1-relaxation time. Interleaved acquisition acts to reduce cross-talk effect (13).

Magnetization transfer (MT) effect may be another reason why interleaved SE T1-weighted imaging offers better GM-WM contrast than sequential imaging at 3 T because sequential imaging has more radiofrequency pulses per TR interval than interleaved imaging. MT effect is an important factor in determining contrast (14,15), and is also a significant contributor to image contrast in multi-slice acquisition compared with single-slice acquisition (15,16), and this effect is stronger at higher fields (16–19). Furthermore, the present study showed that application of PP significantly reduced CNR_{GM-WM}. This could also be due to the MT effect caused by PP pulses. CNR_{GM-WM} reduction rate by the application of PP became less prominent with increased number of interleaved samplings. This could be explained that less number of imaging slices for each interleaved image acquisition leads to less MT effect caused by PP. We should be aware of prominent contrast reduction by the application of PP, especially in sequential and 100% interleaved sequences.

An advantage of SE T1-weighted imaging over GRE T1-weighted imaging is that intra-arterial signals are displayed as hypointense due to the flow-void effect, which enables differentiation between arterial flow and intra-arterial subacute clots. SE T1-weighted imaging at lower fields is thus well known as a useful sequence in diagnosing vascular lesions, such as arterial dissection (20) and intra-arterial thrombus (particularly subacute phase). SE T1-weighted imaging plays a complementary role in relation to MR angiography because MR angiography can misidentify high-intensity thrombus as flow in arteriovenous malformation, and methemoglobin in subacute thrombus can be hyperintense on source images of

Table 1
Vertebral and Basilar Intra-arterial Signal Grade in 18 Volunteers

	Sequential		100% Interleaved		200% Interleaved	
	Without PP	With PP	Without PP	With PP	Without PP	With PP
Vertebral artery						
Grade 0	1 (6)	18 (100)	1 (6)	18 (100)	1 (6)	18 (100)
Grade 1	2 (11)	0 (0)	4 (22)	0 (0)	4 (22)	0 (0)
Grade 2	15 (83)	0 (0)	13 (72)	0 (0)	13 (72)	0 (0)
P value	<.0001		<.0001		<.0001	
Basilar artery						
Grade 0	0 (0)	18 (100)	1 (6)	18 (100)	1 (6)	18 (100)
Grade 1	10 (56)	0 (0)	4 (22)	0 (0)	4 (22)	0 (0)
Grade 2	8 (44)	0 (0)	13 (72)	0 (0)	13 (72)	0 (0)
P value	<.0001		<.0001		<.0001	

Vertebral and basilar intra-arterial signal grading with or without presaturation pulse (PP). Grade 0, no signal; grade 1, mixed signals; grade 2, entirely hyperintense signal. Intra-arterial signals were significantly diminished by application of PP. Percentages are shown in parentheses.

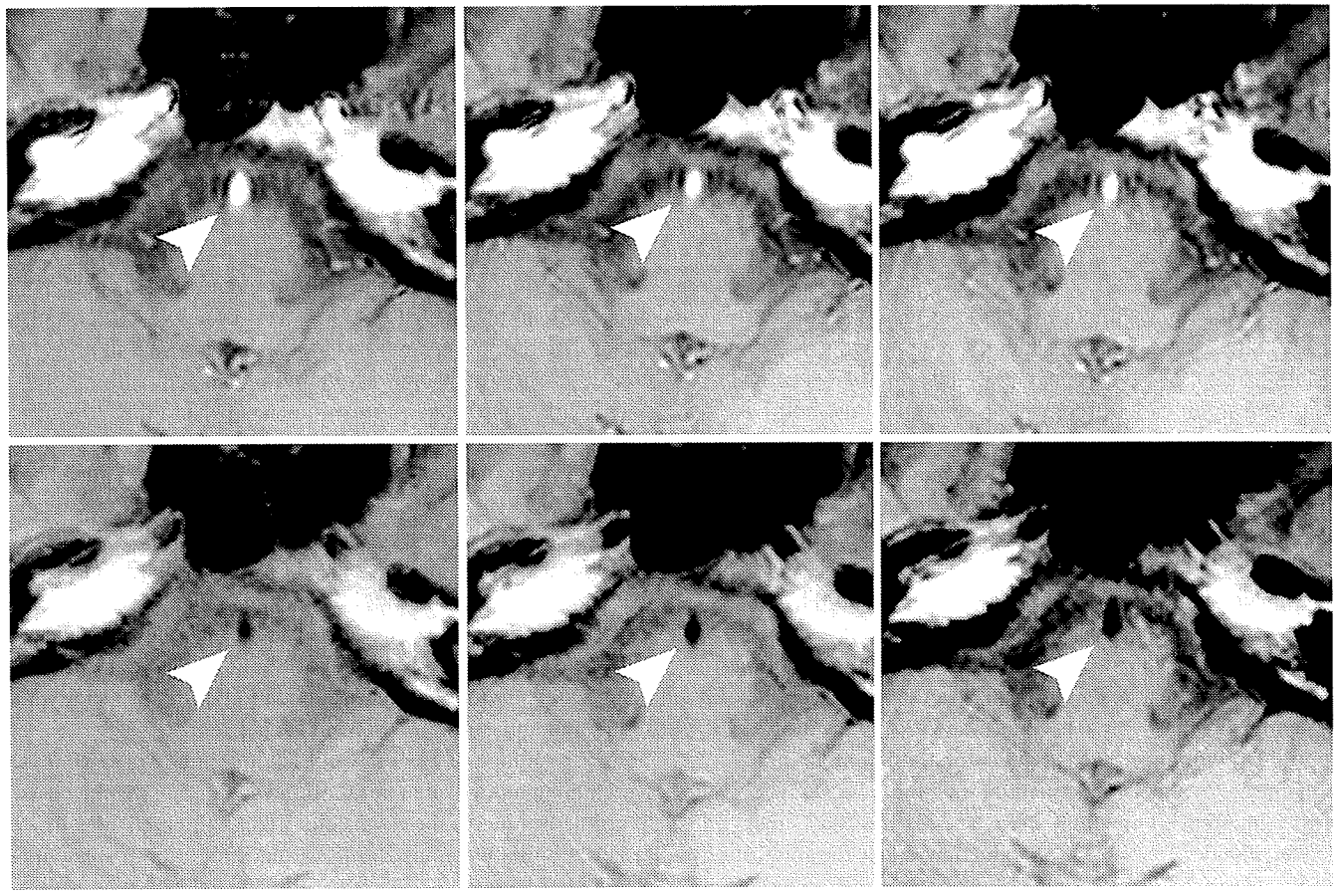

Figure 5. Spin-echo T1-weighted gapless multi-slice imaging at 3 T without presaturation pulse (PP) (*upper row*) and with PP (*lower row*) at the level of the pons. From left to right, sequential imaging, 100% interleaved imaging and 200% interleaved imaging are displayed. Basilar intra-arterial signals were sufficiently suppressed on imaging with PP (*lower row*).

MR angiography (9,21). At high fields such as 3 T, intra-arterial blood tends to be hyperintense because of increased paradoxical enhancement due to longer T1 relaxation time. In fact, in the present study, vertebral and basilar intra-arterial signals were displayed as hyperintense or mixed signals in ≥94% (17 of 18) of volunteers on all three types of imaging without PP. Consequently, SE T1-weighted imaging without PP may not be able to reveal some vascular diseases, such as

arterial dissection or intra-arterial thrombus. However, these vertebral and basilar intra-arterial signals were completely suppressed by PP, as shown in the current study. The present study demonstrated that PP effectively suppresses intra-arterial signal, even at 3 T.

Another advantage of SE sequence over GRE sequence in obtaining T1-weighted imaging is that SE imaging displays significantly fewer susceptibility artifacts than GRE imaging (8). Susceptibility artifacts degrade image quality at air/tissue interfaces, such as paranasal sinuses, temporal bone, and the pituitary gland (22,23). Furthermore, susceptibility artifacts are more enhanced at higher field strength (24,25). SE imaging would thus be more suitable than GRE imaging in evaluating lesions near air/tissue interfaces, such as pituitary adenoma at 3 T.

This study has several limitations. We have not optimized the imaging parameters, such as TR, TE, or slice thickness. Further studies are needed to optimize SE T1-weighted imaging parameters at 3 T for clinical use. Further studies are also needed to verify the usefulness of interleaved SE T1-weighted imaging with PP in diagnosing diseases, such as arterial dissection or pituitary adenoma, in which SE T1-weighted imaging has been reported as useful at lower fields. We did not analyze the contrast on T1-weighted fluid-attenuated inversion recovery (FLAIR) sequence. A previous study at 0.2T showed that T1-weighted FLAIR images had better CNR of GM-WM than SE T1-weighted images (26). However, another previous study at 1.5 T showed no significant difference in CNR of peripheral GM-WM between T1-weighted FLAIR and SE T1-weighted images (27). Contrast on T1-weighted FLAIR images may be affected by segmentation of the k-space due to multiple TEs and by increased MT effect attributable to multiple refocusing pulses. Future studies may be needed to quantitatively compare the contrast between GM and WM on SE T1-weighted sequence and T1-weighted FLAIR sequence at 3 T.

CONCLUSION

This study revealed that GM-WM contrast on SE T1-weighted imaging at 3 T can be improved by interleaved acquisition, and that PP satisfactorily suppresses intra-arterial signals. Interleaved SE T1-weighted imaging with PP could be clinically feasible at 3 T.

REFERENCES

1. Nobauer-Huhmann IM, Ba-Ssalamah A, Mlynarik V, et al. Magnetic resonance imaging contrast enhancement of brain tumors at 3 tesla versus 1.5 tesla. Invest Radiol 2002; 37:114–119.
2. Sasaki M, Inoue T, Tohyama K, et al. High-field MRI of the central nervous system: current approaches to clinical and microscopic imaging. Magn Reson Med Sci 2003; 2:133–139.
3. Scarabino T, Nemore F, Giannatempo GM, et al. 3.0 T magnetic resonance in neuroradiology. Eur J Radiol 2003; 48:154–164.
4. Ross JS. The high-field-strength curmudgeon. AJNR Am J Neuroradiol 2004; 25:168–169.
5. Kuhl CK, Traber F, Schild HH. Whole-body high-field-strength (3.0-T) MR imaging in clinical practice. Part I. Technical considerations and clinical applications. Radiology 2008; 246:675–696.
6. Schmitz BL, Gron G, Brausewetter F, et al. Enhancing gray-to-white matter contrast in 3 T T1 spin-echo brain scans by optimizing flip angle. AJNR Am J Neuroradiol 2005; 26:2000–2004.
7. Lu H, Nagae-Poetscher LM, Golay X, et al. Routine clinical brain MRI sequences for use at 3.0 Tesla. J Magn Reson Imaging 2005; 22:13–22.
8. Farahani K, Sinha U, Sinha S, et al. Effect of field strength on susceptibility artifacts in magnetic resonance imaging. Comput Med Imaging Graph 1990; 14:409–413.
9. Yousem DM, Balakrishnan J, Debrun GM, et al. Hyperintense thrombus on GRASS MR images: potential pitfall in flow evaluation. AJNR Am J Neuroradiol 1990; 11:51–58.
10. Fushimi Y, Miki Y, Urayama S, et al. Gray matter-white matter contrast on spin-echo T1-weighted images at 3 T and 1.5 T: a quantitative comparison study. Eur Radiol 2007; 17:2921–2925.
11. Felmlee JP, Ehman RL. Spatial presaturation: a method for suppressing flow artifacts and improving depiction of vascular anatomy in MR imaging. Radiology 1987; 164:559–564.
12. U.S. Department of Health and Human Services FDA, Center for Devices and Radiological Health Guidance for Industry and FDA Staff-Criteria for Significant Risk Investigations of Magnetic Resonance Diagnostic Devices. 2003. Available at:http://www.fda.gov/cdrh/ode/guidance/793.html. Accessed February 5, 2009.
13. Kneeland JB, Shimakawa A, Wehrli FW. Effect of intersection spacing on MR image contrast and study time. Radiology 1986; 158:819–822.
14. Majumdar S, Sostman HD, MacFall JR. Contrast and accuracy of relaxation time measurements in acquired and synthesized multislice magnetic resonance images. Invest Radiol 1989; 24:119–127.
15. Watanabe A, Boesch C, Obata T, et al. Effect of multislice acquisition on T1 and T2 measurements of articular cartilage at 3 T. J Magn Reson Imaging 2007; 26:109–117.
16. Chang Y, Bae SJ, Lee YJ, et al. Incidental magnetization transfer effects in multislice brain MRI at 3.0 T. J Magn Reson Imaging 2007; 25:862–865.
17. Duvvuri U, Roberts DA, Leigh JS, et al. Magnetization transfer imaging of the brain: A quantitative comparison of results obtained at 1.5 and 4.0 T. J Magn Reson Imaging 1999; 10:527–532.
18. Melhem ER, Jara H, Yucel EK. Multislice T1-weighted hybrid RARE in CNS imaging: assessment of magnetization transfer effects and artifacts. J Magn Reson Imaging 1996; 6:903–908.
19. Schmitz BL, Aschoff AJ, Hoffmann MH, et al. Advantages and pitfalls in 3 T MR brain imaging: a pictorial review. AJNR Am J Neuroradiol 2005; 26:2229–2237.
20. Mascalchi M, Bianchi MC, Mangiafico S, et al. MRI and MR angiography of vertebral artery dissection. Neuroradiology 1997; 39:329–340.
21. Hirabuki N, Fujita N, Hashimoto T, et al. Follow-up MRI in dural arteriovenous malformations involving the cavernous sinus: emphasis on detection of venous thrombosis. Neuroradiology 1992; 34:423–427.
22. Oehler MC, Schmalbrock P, Chakeres D, et al. Magnetic susceptibility artifacts on high-resolution MR of the temporal bone. AJNR Am J Neuroradiol 1995; 16:1135–1143.
23. Sakurai K, Fujita N, Harada K, et al. Magnetic susceptibility artifact in spin-echo MR imaging of the pituitary gland. AJNR Am J Neuroradiol 1992; 13:1301–1308.
24. Abduljalil AM, Robitaille PM. Macroscopic susceptibility in ultra high field MRI. J Comput Assist Tomogr 1999; 23:832–841.
25. Abduljalil AM, Kangarlu A, Yu Y, et al. Macroscopic susceptibility in ultra high field MRI. II: acquisition of spin echo images from the human head. J Comput Assist Tomogr 1999; 23:842–844.
26. Hori M, Okubo T, Uozumi K, et al. T1-weighted fluid-attenuated inversion recovery at low field strength: a viable alternative for T1-weighted intracranial imaging. AJNR Am J Neuroradiol 2003; 24:648–651.
27. Alibek S, Adamietz B, Cavallaro A, et al. Contrast-enhanced T1-weighted fluid-attenuated inversion-recovery BLADE magnetic resonance imaging of the brain: an alternative to spin-echo technique for detection of brain lesions in the unsedated pediatric patient? Acad Radiol 2008; 15:986–995.

Original Research

Visualization of the Lenticulostriate Artery With Flow-Sensitive Black-Blood Acquisition in Comparison With Time-of-Flight MR Angiography

Kimio Gotoh, MD,[1] Tomohisa Okada, MD, PhD,[1]* Yukio Miki, MD, PhD,[1] Masato Ikedo, BS,[2] Ayako Ninomiya, RT,[2] Toshikazu Kamae, MS,[1] and Kaori Togashi, MD, PhD[1]

Purpose: To evaluate the capability of flow-sensitive black blood (FSBB) acquisition to visualize the lenticulostriate artery (LSA) in comparison with time-of-flight (TOF) angiography.

Materials and Methods: Twenty-one healthy subjects (13 males and 8 females, 19–44 years old) were enrolled in this study after obtaining written informed consent. Magnetic resonance imaging (MRI) examinations were performed with FSBB and TOF to visualize the LSA using a 1.5T MRI unit. In FSBB acquisition a motion probing gradient of b = 4 sec/mm^2 was applied to dephase blood flow. Images were reconstructed into coronal sections and were evaluated in terms of number, length, and image quality at origins and distal areas of visualized LSA branches with a four-point scale.

Results: In all, 145 LSA branches were visualized with FSBB and 66 branches with TOF. There was no LSA visualized only with TOF. In all evaluated terms, FSBB was significantly better than TOF.

Conclusion: We could better visualize the LSA with FSBB than with TOF, both quantitatively and qualitatively. FSBB is a promising method, although it remains to be evaluated in clinical cases.

Key Words: lenticulostriate artery; flow-sensitive black blood; time-of-flight; MR angiography; diffusion
J. Magn. Reson. Imaging 2009;29:65–69.

THE LENTICULOSTRIATE ARTERY (LSA) originates mainly from the middle cerebral artery (MCA) and supplies blood to the basal ganglia and the internal capsule (1,2). Its occlusion results in lacunar infarct (3,4). In some of these patients, linear structures with abnormal density or signal were observed, consistent with occluded perforating arteries associated with the relevant lacunar infarct (5). In a prospective study of 93 patients of small subcortical infarcts, some relevance to MCA stenosis was observed but about 60% of cases were free of it (6). The LSA plays an important role for vascular disease at basal ganglia; however, its noninvasive visualization was limited.

Recently, susceptibility-weighted imaging (SWI) has been introduced as one of the ways of observing small vessels as black blood (7–9). In SWI, however, the flow rephasing is implemented and phase disturbance is observed mainly in the vein and its power for visualization of the artery is limited. On the other hand, signal from flowing blood can be attenuated by applying very weak motion probing gradients (dephase gradients), which mainly attenuates signal from moving blood in the artery and capillary, as well as in the vein (10), while the signal of the stationary component is almost intact, unlike diffusion-weighted images for stroke examination acquired with much larger motion probing gradients (MPGs). One such method proposed is flow-sensitive black blood (FSBB) acquisition (11,12).

Dilated LSA branches were visualized noninvasively with time-of-flight (TOF) MR angiography (MRA) in moya-moya patients (13). The TOF-MRA may visualize some branches of the LSA without dilatation, but invasive angiography is used for clinical evaluation (14) and the capability has not been much investigated.

From these considerations we hypothesized that the LSA would be better visualized with FSBB acquisition than with TOF-MRA and the purpose of this study was to examine and illustrate the advantage of using FSBB in comparison with TOF for visualization of the LSA.

MATERIALS AND METHODS

Subjects

Twenty-one healthy volunteers (13 males and 8 females; range 19–44 years old, mean 25 years old) with-

[1]Department of Diagnostic Radiology, Kyoto University Graduate School of Medicine, Kyoto, Japan.
[2]Toshiba Medical Systems Corp., Otawara-shi, Japan.
Contract grant sponsor: R&D of Molecular Imaging Equipment for Malignant Tumor Therapy Support, supported by New Energy and Industrial Technology Development Organization in Japan.
*Address reprint requests to: T.O., Department of Diagnostic Radiology, Kyoto University Graduate School of Medicine, 54 Shogoin Kawaharacho, Sakyoku, Kyoto, 606–8507, Japan. E-mail: tomokada@kuhp.kyoto-u.ac.jp
Received June 24, 2008; Accepted September 10, 2008.
DOI 10.1002/jmri.21626
Published online in Wiley InterScience (www.interscience.wiley.com).

out any known disease were enrolled in this study after obtaining written informed consent, based on the protocol approved by the Institutional Review Board.

Image Acquisition

The subjects were examined with both FSBB and TOF methods in order to visualize the LSA on a 1.5T MRI unit (EXCELART Vantage Powered by ATLAS, Toshiba Medical Systems, Otawara-shi, Japan). After obtaining localizing images of three orthogonal axis, T2-weighted fast spin echo images were acquired parallel to the AC (anterior commissure)-PC (posterior commissure) with the following parameters: TR/TE 4000/105 msec, flip angle 90/160°, acquisition matrix size 320 × 256, field of view (FOV) 220 × 180 mm, slice thickness 3 mm with 0.6 mm gap in 40 slices to cover the whole brain. In the same AC-PC slice orientation, TOF-MRA and FSBB images were scanned using the 3D gradient echo acquisition. The common imaging parameters were TR 29 msec, flip angle 20°, acquisition matrix size 256 × 224, FOV 205 × 179 mm in one axial 3D slab of 160 slices. The scan resolution was 0.8 × 0.8 × 0.8 mm, which was interpolated into 0.4 × 0.4 × 0.4 mm in order to increase apparent resolution and improve image quality after reformatting. The scan time was 6 minutes 35 seconds. In the TOF scan, TE was 6.8 msec and a magnetization transfer contrast pulse and flow rephasing were used. For the FSBB acquisition, TE was 20 msec and the motion probing gradient of b = 4 sec/mm^2 was evenly divided and applied to all three axes. At the initial stage we evaluated effect of MPG at different b values of 0, 1, 2, and 4 sec/mm^2 as a preliminary evaluation.

Image Analysis

The 3D image volume data was transferred to a commercially available workstation (AZE VirtualPlace Lexus, AZE, Tokyo, Japan) and the following processings and evaluations were conducted on the same workstation. After reorienting the 3D axial image volumes into coronal (perpendicular to the AC-PC line), each of five consecutive slices was projected by maximum intensity (ie, MIP of 2 mm thickness) for TOF and by minimum intensity (ie, MinIP of 2 mm thickness) for FSBB. By using these images, LSA branches were traced and measured for length on the workstation. On the reconstructed images, LSA branches longer than 5 mm were analyzed. When an artery branches within 5 mm from the MCA origin, each branch was counted and measured separately, because more than 70% of branches were found to originate from common trunks (1). When an artery branches at a more distal site, only the longest branch was counted and measured. Images were analyzed in terms of number, length, and quality of visualization for the visualized LSA branches using a four-point scale (0: not visualized, 1: poor, 2: good, and 3: excellent). The quality of visualization was evaluated separately at origins of the LSA and areas distal to them. The evaluation was performed for each and every visualized LSA branches in random order by two experienced radiologists in consensus, although we could not avoid evaluators noticing the acquisition method due to differences in appearance between FSBB and TOF images. The length of LSA branches was measured by another researcher. On the T2-weighted axial images, high-intensity spots were examined in the basal ganglia region above the anterior perforated substance and the number of the perivascular space was counted by two radiologists in consensus.

Statistical Analysis

The numbers of visualized branches per subject were compared between FSBB and TOF with a two-tailed paired *t*-test, separately for left and right hemispheres. The difference in numbers between left and right was also examined. Lengths of all visualized LSA branches were compared between FSBB and TOF with a two-tailed two-sample *t*-test. In the comparisons of scores for quality of visualization between FSBB and TOF, a Wilcoxon signed rank test was used. A *P*-value less than 0.05 was considered statistically significant. Statistical analyses were conducted using a commercially available software package (SPSS 16.0, SPSS, Chicago, IL).

RESULTS

Preliminary Evaluation

FSBB acquisitions were performed, with a certain range of b values (b = 0, 1, 2, and 4 s/mm^2; the last value was the maximum in the system). Representative images are shown in Fig. 1. Very few LSAs were visualized at b = 0 s/mm^2 and more of them were better depicted according to the increase of b values. Visualization was best at a b value of 4 s/mm^2, which was adopted for the current study.

Number and Length of Visualized LSAs

The average numbers and standard deviations of visualized LSAs per subject were 3.6 ± 1.2 and 1.5 ± 0.8 on the left, and 3.3 ± 1.0 and 1.7 ± 0.9 on the right for FSBB and TOF, respectively (Table 1). The differences between FSBB and TOF were significant ($P = 0.001$) on both sides; however, there was no significant difference between left and right for both FSBB and TOF ($P = 0.459$ and $P = 0.479$, respectively). The total number of branches visualized with FSBB was 145, and 66 (46%) were also visualized with TOF. There was no LSA that was visible only in TOF images. The average lengths of visualized LSA branches were 21.8 ± 7.1 mm and 18.6 ± 8.1 mm for FSBB and TOF, respectively (Table 1), which were statistically significantly different ($P = 0.008$). Some representative images are presented in Fig. 2 using thicker projected images (8 mm) than those used for analysis.

Quality of Visualization at Origins and Areas Distal to Them

Visualization scores are summarized in Table 2. At the origin of LSA branches, FSBB showed significantly better visualization of the LSA than TOF ($P = 0.003$). Also, at the areas distal to the origins, FSBB was better than TOF ($P = 0.001$). The results of the number, length, and

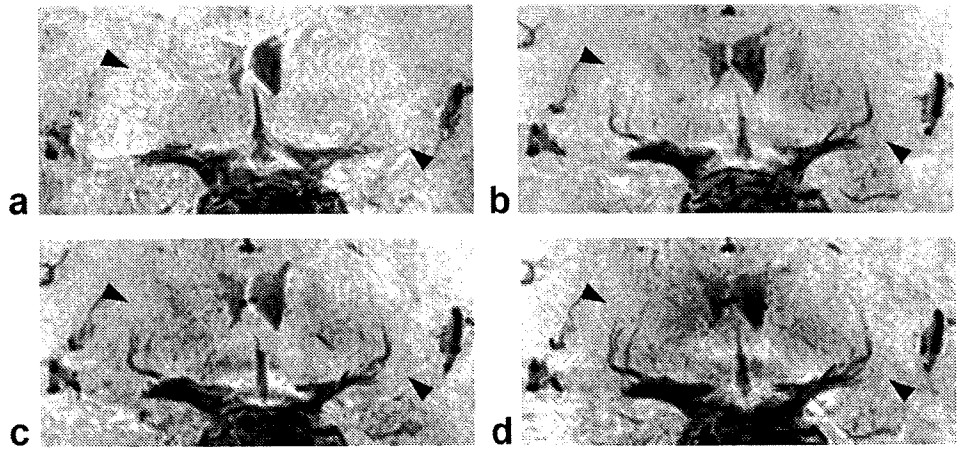

Figure 1. Differences in visualization of the lenticulostriate artery (LSA) dependent on the b values of motion probing gradient (MPG): b = 0, 1, 2, and 4 s/mm^2, as presented in images **(a–d)**, respectively. Better visualization of LSA is observed (see arrowheads) by increasing b values, whereas CSF signal is gradually decreased.

quality of visualization at distal areas for LSA branches visualized with FSBB and TOF are illustrated in Fig. 3.

Number of the Perivascular Space and Other Lesions on T2WI

No significantly abnormal finding was detected on T2WIs of all the subjects. The perivascular spaces were detected as tiny high intensity spots on axial T2WIs above the anterior perforated substance in some subjects, but the number was 7 in total and they were limited 1 to 2 slices above the slice with the anterior perforated substance.

DISCUSSION

Histological examination of the LSAs in the vascular casts of 48 middle cerebral arteries revealed that more than 90% of LSA branches originated from the first segment of the MCA (M1), and they ranged between 2 and 12 (mean 7.1) in number and from 80 μm to 1,400 μm in size (1). Another study reported that there were usually three branches in the middle group and one to nine in the lateral group (2). By using the FSBB method, we observed 3.6 and 3.3 branches on average on the left and right sides, respectively. These results conform to the aforementioned histological results. Although the whole branches of the LSA may not be visualized even with FSBB acquisition, length and quality of visualization were significantly better with FSBB scan than TOF-MRA, which requires rapid vascular inflow (15), and LSA branches were considered to be too small to fully visualize with the latter method. On the other hand, even slow flow can be dephased by a weak motion probing gradient and the FSBB acquisition was more sensitive in detecting small vessels with slow flow like the LSA. Although FSBB is suitable for visualizing small arteries, it might be used to evaluate a larger artery with turbulent flow. In patients with sickle cell disease, high-velocity flow secondary to anemia generates turbulence and it produces intimal injury and hyperplasia, resulting in infarction. But at the same time, this turbulence often causes pseudo-lesion on TOF-MRA (16). Although such cases are yet to be evaluated, intimal hyperplasia might show some signal on the FSBB image and it may help to avoid pseudo-lesions. In the FSBB image the perivascular space or cerebrospinal fluid (CSF) might possibly be detected as the same signal void. However, it should be noted that the number of the perivascular space detected on the T2WI was 7 in the whole subjects and they were limited within one or two slices above the anterior perforated substance. In aged subjects, the perivascular space would frequently be dilated, but CSF signal in the space is expected to be higher than LSA signal, which is void, as shown in Figs. 1 and 2. Calcification, small hemorrhage, and iron deposit would be visualized as signal void, but they would be identified as spotty, nodular, or even mass-like lesions and may not be recognized as "string-like" LSAs.

Table 1
Number and Length of Visualized LSA Branches

	Numbers		Length
	Left	Right	
FSBB	3.6 ± 1.2	3.3 ± 1.0	21.8 ± 7.1 (145)
TOF	1.5 ± 0.8	1.7 ± 0.9	18.6 ± 8.1 (66)
P value	*P* = 0.001	*P* = 0.001	*P* = 0.008

Numbers and length are presented in mean ± standard deviation, and total branch numbers are presented in parentheses.

Quality of visualization was evaluated at the origin of LSA branches, because understanding the microanatomy of the proximal middle cerebral artery (M1) and its branches is very important for aneurysm surgery. It may cause clipping or blood flow disturbance of LSA, resulting in cerebral infarction (17,18). Although aneurysm clipping is generally preceded by digital subtraction angiography (DSA), not all hospitals can use 3D-DSA. 3D and isotropic information of the FSBB image may complement bi-plane DSA. The average scores for the FSBB image were lower compared with those evaluated at distal areas. It was probably caused by the pulsatile motion of CSF, because gross motion causes signal reduction by MPG even at a b value of 4 s/mm^2. Hence, for better visualization at the origin a lower b value would be appropriate.

In the analysis axial slabs were reformatted into the coronal orientation and every five slices were projected and reconstructed as one slice of 2 mm thickness for minimum intensity in the FSBB images and for maximum intensity in the TOF images. Although thicker

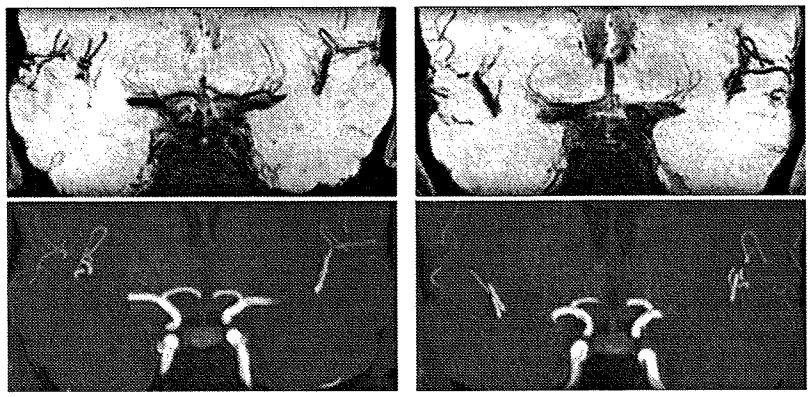

Figure 2. Representative images of LSA branches from two subjects (left and right columns). The upper row shows FSBB images and the lower shows TOF images. Better visualization is noted in images of FSBB than TOF.

slices allowed easier detection, measurement, and evaluation of the LSA, they might yield more errors, because LSA branches looked as if they were fusing each other when viewed on thick slices despite the observation that their anastomosis is very rare (19). On the other hand, when the slice was very thin tracing the continuity of an LSA branch was difficult and it caused some errors in measuring the entire length that was visualized. Hence, a minimum intensity projection of 2 mm slice thickness was adopted for better processing. For viewing purposes, however, thicker reformatting would be useful, as illustrated in Fig. 2 (8 mm thick).

In a series of cases with a small infarct in the territory of the LSAs more than 75% of the patients were either hypertensive or diabetic (20), both of which increase the risk of cerebrovascular disease, including in the areas of deep brain structures. For these patients, screening for abnormal findings of the LSA could be beneficial, as TOF-MRA has been made great contributions to completely noninvasive screening for abnormality of vasculatures of larger size. Cerebral hemorrhage in basal ganglia is also associated with LSA abnormalities, such as dissection, aneurysm, and abnormal dilatation. The microaneurysm of perforating arteries was suggested to be responsible for hypertension-induced cerebral hemorrhage (21). If some morphological changes in the LSA, such as hypovisualization, left–right asymmetry, and an aneurysm are visualized in asymptomatic patients of DM or hypertension, it may allow more rigorous therapeutic interventions to prevent symptomatic events, although further studies are required to clarify a causality linkage between FSBB findings and future morbidity. The noninvasive nature of FSBB acquisition would also enable regular follow-up observations. The FSBB acquisition is a noninvasive modality and may play an important role in assessing the LSA.

There are some limitations in this study. First, almost all the subjects were younger than 40 years old and the range of subject age was limited because this study intended to evaluate the feasibility of FSBB acquisition to visualize the LSA. Further studies on patients of lacunae, DM, hypertension, and others are yet to be made. Second is the absence of a reference standard. Conventional angiography may better visualize the LSA; however, angiographic images of healthy volunteers were not obtainable because the procedure is invasive and has some risk of complications. Lastly, FSBB is better at visualizing small and slow-flow arteries. For larger arteries, TOF visualizes better and is suitable for multidirectional MIP observation. Therefore, FSBB should be used complementary to TOF.

Table 2
Visualization Scores for LSA Branches

	FSBB	TOF
Origin		
3	43	16
2	66	17
1	34	25
0	2	8
Total	145[a]	66
Distal area		
3	67	7
2	64	28
1	14	31
Total	145[b]	66

[a]$P = 0.003$, [b]$P = 0.001$.

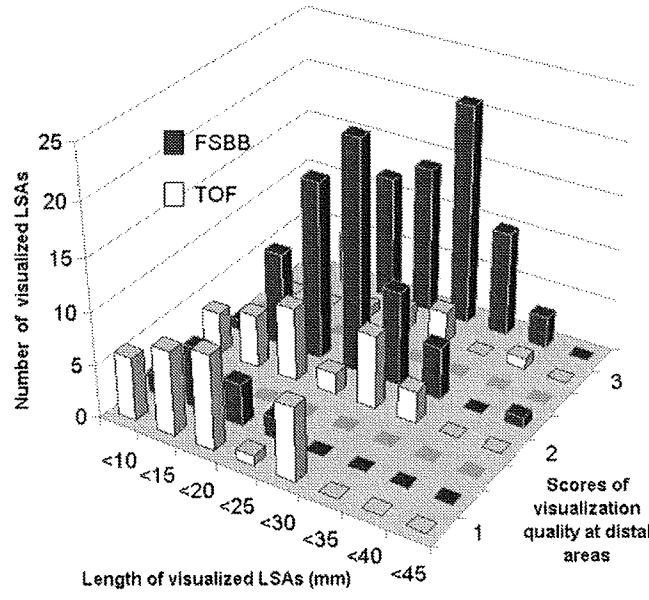

Figure 3. A histogram presentation of numbers, length, and quality scores at distal areas for 145 and 66 LSA branches visualized by FSBB and TOF, respectively. It is illustrated that FSBB visualized longer at higher quality than TOF.

In conclusion, we could better visualize the LSA with FSBB acquisition than with TOF-MRA, both quantitatively and qualitatively. The FSBB scan is considered a promising method, but it remains to be evaluated in clinical cases.

REFERENCES

1. Marinkovic S, Gibo H, Milisavljevic M, Cetkovic M. Anatomic and clinical correlations of the lenticulostriate arteries. Clin Anat 2001; 14:190–195.
2. Marinkovic SV, Kovacevic MS, Marinkovic JM. Perforating branches of the middle cerebral artery. Microsurgical anatomy of their extracerebral segments. J Neurosurg 1985;63:266–271.
3. Feekes JA, Hsu SW, Chaloupka JC, Cassell MD. Tertiary microvascular territories define lacunar infarcts in the basal ganglia. Ann Neurol 2005;58:18–30.
4. Feekes JA, Cassell MD. The vascular supply of the functional compartments of the human striatum. Brain 2006;129:2189–2201.
5. Wardlaw JM, Dennis MS, Warlow CP, Sandercock PA. Imaging appearance of the symptomatic perforating artery in patients with lacunar infarction: occlusion or other vascular pathology? Ann Neurol 2001;50:208–215.
6. Wang X, Lam WW, Fan YH, Graham CA, Rainer TH, Wong KS. Topographic patterns of small subcortical infarcts associated with MCA stenosis: a diffusion-weighted MRI study. J Neuroimaging 2006;16:266–271.
7. Haacke EM, Xu Y, Cheng YC, Reichenbach JR. Susceptibility weighted imaging (SWI). Magn Reson Med 2004;52:612–618.
8. Reichenbach JR, Barth M, Haacke EM, Klarhofer M, Kaiser WA, Moser E. High-resolution MR venography at 3.0 Tesla. J Comput Assist Tomogr 2000;24:949–957.
9. Wang Y, Yu Y, Li D, et al. Artery and vein separation using susceptibility-dependent phase in contrast-enhanced MRA. J Magn Reson Imaging 2000;12:661–670.
10. Le Bihan D, Breton E, Lallemand D, Aubin ML, Vignaud J, Laval-Jeantet M. Separation of diffusion and perfusion in intravoxel incoherent motion MR imaging. Radiology 1988;168:497–505.
11. Kimura T, Ikedo M, Furudate N, Takemoto S. Flow-sensitive susceptibility-weighted imaging. In: Proc Joint Annual Meeting ISMRM-ESMRMB, Berlin; May 19–25, 2007:3015.
12. Tsuchiya K, Tateishi H, Yoshida M, et al. Flow-sensitive susceptibility-weighted imaging of the brain: initial experience in ischemic lesions. In: Proc Joint Annual Meeting ISMRM-ESMRMB, Berlin; May 19–25, 2007:3016.
13. Fushimi Y, Miki Y, Kikuta K, et al. Comparison of 3.0- and 1.5-T three-dimensional time-of-flight MR angiography in moyamoya disease: preliminary experience. Radiology 2006;239:232–237.
14. Nakano S, Iseda T, Kawano H, Yoneyama T, Ikeda T, Wakisaka S. Correlation of early CT signs in the deep middle cerebral artery territories with angiographically confirmed site of arterial occlusion. AJNR Am J Neuroradiol 2001;22:654–659.
15. Bradley WG Jr, Waluch V. Blood flow: magnetic resonance imaging. Radiology 1985;154:443–450.
16. Gillams AR, McMahon L, Weinberg G, Carter AP. MRA of the intracranial circulation in asymptomatic patients with sickle cell disease. Pediatr Radiol 1998;28:283–287.
17. Sasaki T, Kodama N, Matsumoto M, et al. Blood flow disturbance in perforating arteries attributable to aneurysm surgery. J Neurosurg 2007;107:60–67.
18. Park DH, Kang SH, Lee JB, et al. Angiographic features, surgical management and outcomes of proximal middle cerebral artery aneurysms. Clin Neurol Neurosurg 2008;110:544–551.
19. Marinkovic S, Milisavljevic M, Marinkovic Z. Anastomoses among the perforating arteries of the brain. Microanatomy and clinical significance. Neurologija 1990;39:107–114.
20. Ghika J, Bogousslavsky J, Regli F. Infarcts in the territory of lenticulostriate branches from the middle cerebral artery. Etiological factors and clinical features in 65 cases. Schweiz Arch Neurol Psychiatr 1991;142:5–18.
21. Ahn JY, Cho JH, Lee JW. Distal lenticulostriate artery aneurysm in deep intracerebral haemorrhage. J Neurol Neurosurg Psychiatry 2007;78:1401–1403.

European Journal of Radiology 73 (2010) 114–118

Contents lists available at ScienceDirect

European Journal of Radiology

journal homepage: www.elsevier.com/locate/ejrad

High spatial resolution 3D MR cholangiography with high sampling efficiency technique (SPACE): Comparison of 3 T vs. 1.5 T

Shigeki Arizono*, Hiroyoshi Isoda, Yoji S. Maetani, Yuusuke Hirokawa, Kotaro Shimada, Yuji Nakamoto, Toshiya Shibata, Kaori Togashi

Department of Diagnostic Imaging and Nuclear Medicine, Kyoto University Graduate School of Medicine, 54 Shogoin Kawahara-cho, Sakyo-ku, Kyoto 606-8507, Japan

ARTICLE INFO

Article history:
Received 4 June 2008
Received in revised form 5 August 2008
Accepted 6 August 2008

Keywords:
High field
3 T
MR cholangiography
SPACE
High resolution
3D

ABSTRACT

Purpose: The aim of this study was to evaluate image quality of 3D MR cholangiography (MRC) using high sampling efficiency technique (SPACE) at 3 T compared with 1.5 T.
Methods and materials: An IRB approved prospective study was performed with 17 healthy volunteers using both 3 and 1.5 T MR scanners. MRC images were obtained with free-breathing navigator-triggered 3D T2-weighted turbo spin-echo sequence with SPACE (TR, >2700 ms; TE, 780 ms at 3 T and 801 ms at 1.5 T; echo-train length, 121; voxel size, 1.1 mm × 1.0 mm × 0.84 mm). The common bile duct (CBD) to liver contrast-to-noise ratios (CNRs) were compared between 3 and 1.5 T. A five-point scale was used to compare overall image quality and visualization of the third branches of bile duct (B2, B6, and B8). The depiction of cystic duct insertion and the highest order of bile duct visible were also compared. The results were compared using the Wilcoxon signed-ranks test.
Results: CNR between the CBD and liver was significantly higher at 3 T than 1.5 T ($p = 0.0006$). MRC at 3 T showed a significantly higher overall image quality ($p = 0.0215$) and clearer visualization of B2 ($p = 0.0183$) and B6 ($p = 0.0106$) than at 1.5 T. In all analyses of duct visibility, 3 T showed higher scores than 1.5 T.
Conclusion: 3 T MRC using SPACE offered better image quality than 1.5 T. SPACE technique facilitated high-resolution 3D MRC with excellent image quality at 3 T.

1. Introduction

Magnetic resonance cholangiography (MRC) has been accepted as a powerful imaging modality for the assessment of biliary disorders [1–5]. However, conventional MRC using the heavily T2-weighted turbo spin-echo (TSE) technique with two-dimensional (2D) thick-slab or 2D multislice at 1.5 T MR units is insufficient to evaluate the intrahepatic bile duct (IHBD), particularly if the biliary system is not dilated, because of limited spatial resolution and the signal-to-noise ratio (SNR) [6–8]. Therefore, the utility of MRC is restricted when detailed anatomic information of the non-dilated IHBD is needed, for example, for the preoperative assessment of living-related liver transplant donors [6,9,10].

Recently, 3 T whole-body MR scanners have been introduced and become available for upper abdominal imaging [11,12]. They can facilitate high-quality MRC, reflecting the abundant SNR. Some investigators have reported that MRC at 3 T has the potential to improve the visualization of anatomic details compared to 1.5 T [7,13,14]. However, specific absorption ratio (SAR) deposition is sometimes problematic at 3 T, which might force us to reluctantly change protocols, especially in three-dimensional (3D) TSE sequence.

To avoid the SAR problem, a new technique of Sampling Perfection with Application optimized Contrasts using different flip angle Evolutions, called SPACE, has been proposed. This sequence is a variant of 3D TSE, and uses a variable flip angle less than 180°, which allows a larger number of refocusing pulses to be used per repetition time while good T2-weighted contrast and low SAR are maintained without reducing a better SNR at 3 T [15–17]. In our previous study, we proved that high spatial resolution 3D MRC with SPACE at 3 T produces higher image quality of the biliary tract compared to 3D MRC with the usual constant flip angle TSE sequence, and has the ability to depict the non-dilated IHBD [18]. Haystead et al. also recently reported the superiority of the SPACE technique over conventional constant flip angle TSE sequence in 3D MRC at 3 T [17]. To the best of our knowledge, however, no report has made a comparison of 3D MRC with SPACE between 3 and 1.5 T. Thus, the aim of this study was to evaluate the image quality of 3D MRC with

* Corresponding author. Tel.: +81 75 751 3419; fax: +81 75 771 9709.
E-mail addresses: arizono@kuhp.kyoto-u.ac.jp (S. Arizono), sayuki@kuhp.kyoto-u.ac.jp (H. Isoda), mbo@kuhp.kyoto-u.ac.jp (Y.S. Maetani), yuusuke@kuhp.kyoto-u.ac.jp (Y. Hirokawa), kotaro@kuhp.kyoto-u.ac.jp (K. Shimada), ynakamo1@kuhp.kyoto-u.ac.jp (Y. Nakamoto), ksj@kuhp.kyoto-u.ac.jp (T. Shibata), ktogashi@kuhp.kyoto-u.ac.jp (K. Togashi).

0720-048X/$ – see front matter © 2008 Elsevier Ireland Ltd. All rights reserved.
doi:10.1016/j.ejrad.2008.08.003

Table 1
MR cholangiography sequence parameters

	3 T	1.5 T
TR (ms)	2987–7699[a]	2727–8109[a]
TE (ms)	780	801
Flip angle (°)	[b]	[b]
Echo-train length	121	121
Parallel acquisition technique factor	3	3
No. of signals acquired	2	2
Field of view (mm)	400	400
Inplane resolution (mm)	1.1 × 1.0	1.1 × 1.0
Slice thickness (mm)	0.84	0.84
Slice number	88	88
Acquisition time (min)	3–6[c]	3–6[c]

[a] TR differs among subjects according to respiratory cycle.
[b] Flip angles of the refocusing pulses are variable. The flip angle evolution in SPACE is calculated in order to achieve a high and nearly constant signal of tissues during large part of signal acquisition.
[c] Acquisition time differs among subjects according to respiratory cycle.

SPACE at 3 T compared to 3D MRC with SPACE at 1.5 T, and to assess the advantage of the SPACE technique for achieving high-resolution 3D MRC at 3 T.

2. Materials and methods

2.1. Study design

In a prospective study, 17 healthy volunteers (11 men, 6 women; age range, 26–57 years; mean age, 37 years) were assigned to undergo MRC on both 3 and 1.5 T MR scanners. All volunteers fasted for at least 5 h before the scan, and were examined in random order on both units within a time interval of 2 h. They did not receive any oral contrast agents to suppress bowel signals.

The local institutional review board first approved all MR imaging examinations, and all volunteers gave their written informed consent before the study protocol commenced.

2.2. MRC protocols

MRC imaging was performed at two different commercially available MR systems in the Magnetom series of Siemens (Erlangen, Germany): Magnetom Trio (3 T) and Magnetom Symphony (1.5 T). At 3 T, an eight-channel transmit–receive phased-array coil was used to obtain the images. At 1.5 T, a six-channel transmit–receive phased-array body coil was used. At 3 T, the images were obtained by placing a dielectric pad with US gel doped with Gd-DTPA (RF cushion; Siemens) in front of the body to prevent B1 inhomegeneity caused by the dielectric effect. Prior to MRC, we performed T1-weighted fast low-angle shot sequences and breath-hold T2-weighted TSE sequences to localize the biliary tree. Free-breathing navigator-triggered 3D T2-weighted TSE imaging with SPACE was used to obtain MRC images at each scanner. The prospective acquisition correction (PACE) technique was used to correct respiratory motion. Phase encoding was performed in the left–right direction. The iPAT reconstruction was performed in one direction in the plane of the image slice in the phase-encoding direction. The GRAPPA algorithm was used for the iPAT, and the coil sensitivity information was based on 24 k-space lines. No half-Fourier or filtering techniques were applied. The imaging protocols at 3 and 1.5 T are shown in Table 1. We performed MRC imaging with the same parameters as much as possible, but some different parameters were adopted due to restriction of the device and the sequences provided by the vendor. All MRC images were obtained in the coronal oblique plane at angles parallel to the hepatic hilum.

2.3. Quantitative image analysis

All quantitative and qualitative assessments of the image quality were performed at a commercially available workstation (Ziostation, Ziosoft, Tokyo, Japan). To quantify the image quality of MRC, the common bile duct (CBD) to liver contrast-to-noise ratio (CNR) was measured. One experienced radiologist (10-year experience) conducted operator-defined region-of-interest (ROI) measurements. The signal intensity (SI) of the CBD was measured for each MRC sequence by defining ROIs. ROIs for the SI of the CBD were at least 5 mm^2 and were chosen in homogeneous, artifact-free areas of the middle CBD. To measure SI and the standard deviation (S.D.) of the liver, a single ROI drawn as large as possible was located in a homogenous portion of the liver and set in an area devoid of vessels and prominent artifacts. Because of the inherent inhomogeneity of iPAT images, we could not directly measure the noise. We calculated the S.D. of the liver as the noise ($S.D._{noise}$) instead.

The CBD to the liver CNR was calculated using the following formula: $CNR = (SI_{CBD} - SI_{liver})/S.D._{noise}$.

2.4. Qualitative image analysis

All MRC images were interpreted independently by two experienced radiologists. One operator had 6 years of experience at the beginning of this study, and the other had 17 year's experience. The radiologists were blinded to imaging parameters. Differences were resolved by consensus. If consensus was not achieved, a third reader (14-year experience) determined the score. Maximum intensity projections (MIPs) were generated from each multislice data set on the workstation, and both the source and MIP images from each sequence were used for data analysis.

Visualization of the third branches of the IHBD (B2, B6, and B8) were graded with the use of a five-point scale (5 = excellent, if the duct (third branch) and its branches (fourth branches) could be clearly seen; 4 = good, if the duct could be seen clearly but its branches were moderately visible; 3 = average, if the duct could be seen with moderate visibility but its branches were observable with only limited visibility; 2 = fair, if the duct was visible but the image of the duct was blurred and its branches could not be seen; and 1 = poor, if the duct could not be seen). We chose B2, B6, and B8 for the grading of IHBD imaging because their identification in the biliary tree was relatively easy (Fig. 1a). The depiction of cystic duct insertion was also graded with the use of a three-point scale (3 = clearly depicted; 2 = seen with moderate clarity; 1 = not visible). The overall image quality was assessed on a five-point scale for delineation of the entire biliary system and the presence of artifacts, noise, or both (5 = excellent; 4 = good; 3 = average; 2 = fair; 1 = poor). The highest order of IHBD visible was also recorded.

2.5. Statistics

Statistical analyses were performed using a commercially available software package (Statview, Version 5.0.1; SAS Institute, Cary, NC, USA). The quantitative and qualitative results were compared using the Wilcoxon signed-ranks test. A p-value of less than 0.05 was taken to indicate a significant difference.

3. Results

MRC imaging was performed safely in all subjects without any complications. No volunteers reported thermal sensations during sequences operating near the maximal SAR. Quantitative and qualitative assessments were performed in all 17 volunteers. The results

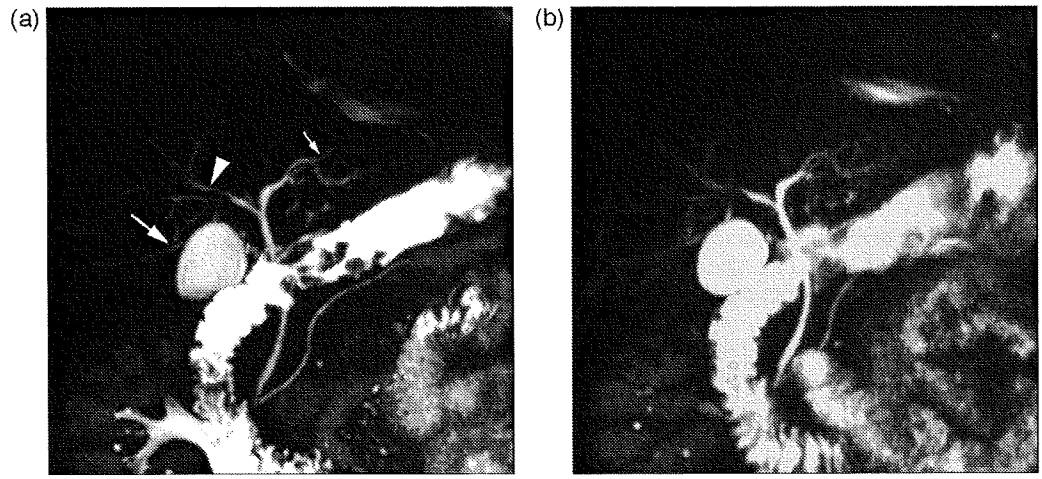

Fig. 1. Comparison of MIP reconstructions of MRC images obtained at 3 T (a) and 1.5 T (b). Third branches of intrahepatic bile ducts are described in (a); B2 (small arrow), B6 (large arrow) and B8 (arrowhead). Visibility of intrahepatic bile ducts was more pronounced on 3 T image.

Table 2
Results of qualitative and quantitative analyses of MRC images obtained at 3 and 1.5 T

	3 T	1.5 T	*p*-Value
CNR between CBD and liver	115 ± 58	75 ± 38	0.0006
B2	3.9 ± 1.3	3.1 ± 1.3	0.0183
B6	3.5 ± 1.4	2.6 ± 1.4	0.0106
B8	4.4 ± 0.9	3.9 ± 1.4	0.1193
Cystic duct insertion	2.6 ± 0.7	2.2 ± 0.8	0.0532
Highest order of IHBD visible	4.2 ± 1.0	3.5 ± 0.9	0.0119
Overall image quality	4.0 ± 1.2	3.1 ± 1.1	0.0215

are summarized in Table 2. Figs. 1 and 2 show examples of MRC images.

3.1. Quantitative image analysis

The CNR between the CBD and liver was 53% higher at 3 T than that at 1.5 T, showing a significant difference.

3.2. Qualitative image analysis

3.2.1. Duct visibility

MRC images obtained at 3 T showed a significantly clearer visualization of B2 and B6 than at 1.5 T. Visualization of B8 showed no significant difference, though the score was higher at 3 T than at 1.5 T. The average of the highest order of IHBD visible on images at 3 T was 4.2 (±1.0); fourth or more peripheral branches of the IHBD were detectable in 13 of 17 volunteers (76%). The result with 1.5 T was 3.5 (±0.9), being significantly inferior to 3 T. In all analyses of duct visibility, MRC images at 3 T showed higher scores than at 1.5 T.

3.2.2. Overall image quality

MRC images obtained at 3 T showed a significantly higher overall image quality than at 1.5 T. Respiratory misregistration was seen in four volunteers; one volunteer in both 3 and 1.5 T images, one in only 3 T images, and two in only 1.5 T images. There were no ghosting or susceptibility artifacts which affected image interpretation on both 3 and 1.5 T images.

4. Discussion

In the present study, we have shown an improvement in image quality on SPACE-using MRC at 3 T compared to 1.5 T. There was also an improvement in the CNR between the CBD and liver. These results are consistent with previous comparison studies of 3D MRC between 3 and 1.5 T. In the study of Merkle et al., involving respiratory-triggered 3D MRC imaging in 15 volunteers, MRC at 3 T offered an improved CNR and a higher level of confidence for

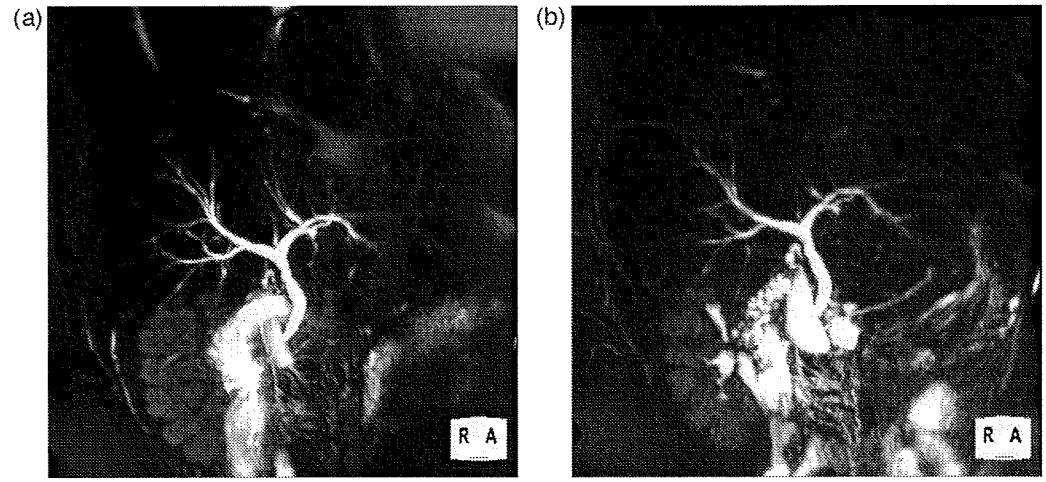

Fig. 2. Other examples of MIP reconstructed MRC images obtained at 3 T (a) and 1.5 T (b). Peripheral intrahepatic bile ducts were excellently depicted on 3 T image.

depicting IHBD variants [7]. Isoda et al. examined 14 volunteers using MRC imaging with respiratory-triggered 3D TSE sequences, and showed that MRC imaging at 3 T provides a significant improvement in duct visibility [14]. In addition to these previous studies, our results suggest the superiority of 3 T MRC over 1.5 T also with the SPACE-using 3D TSE sequence. In contrast, according to Schindera et al., who evaluated two different groups of subject each contained 50 patients at 3 and 1.5 T using MRC with respiratory-triggered 3D TSE, qualitative image analyses did not reveal any significant preference for either field strength [19]. However, 1.5 T sequences may have been closer to the optimum, whereas 3 T sequences were relatively immature, as they discussed in their report.

The present study also revealed that the visibility of the IHBD was markedly enhanced at 3 T. Visualizations of B2 and B6 were significantly better at 3 T compared to 1.5 T, while B8 showed no significant difference. It is possible to assume that abundant SNR at 3 T serves to clearly delineate ducts with a small caliber; generally, B2 and B6 have a smaller caliber compared to B8. At 1.5 T, it is difficult to ensure a sufficient CNR between a small amount of bile fluid and the liver, especially under high-resolution conditions, as in our study. In contrast, the larger caliber of B8 might push up the average scores on both 3 and 1.5 T, which we surmise made difficult to reveal statistically significant difference; indeed the average scores of B8 were higher than B2 and B6 at both 3 and 1.5 T. Because the scores of B8 were also higher at 3 T than at 1.5 T to some extent, further MRC studies involving larger groups could indicate the significant superiority of 3 T over 1.5 T in the visibility of B8.

The improvement in the visibility of the small caliber IHBD was, we assume, achieved by a favorable balance between a high spatial resolution and high SNR. Generally, in upper abdominal imaging at 3 T, the increased SAR is problematic, especially in TSE sequences with long echo trains, because of the high RF power deposition caused by multiple refocusing pulses; this is one of the drawbacks of 3 T. To avoid this, protocol adjustments are often needed, such as decreases in the spatial resolution, number of slices, or the flip angle. These adjustments are undesirable because they reduce resolution and anatomic coverage, alter the contrast, or reduce the signal gain [12,20]. SPACE can overcome these problems and ensure high-resolution images without a decrease in the SNR. In the imaging sequences of the present study, the adopted resolution involved a 1.1 mm × 1.0 mm × 0.84 mm voxel size with 88 slices. This is a higher resolution and larger anatomic coverage than in previous studies of 3D MRC with conventional constant flip angle TSE sequences at 3 T. In these studies, the adopted parameters were: voxel size, 1.35 mm × 1.17 mm × 1 mm; 60 slices [7]: voxel size (before zero-fill interpolation processing), 1.06 mm × 1.06 mm × 1.2 mm; 48 slices [14]: voxel size, 1.25 mm × 1.17 mm × 1 mm; 60 slices [19]: and voxel size (before interpolation processing), 1.25 × 1.17 × 2.0 mm; 72 slices with an interpolated section of 1 mm [17]. These are, respectively, 71, 46, 58, and 217% larger in voxel size, and 19, 22, 19, and 3% smaller in coverage volume compared to our study. In addition, Isoda et al. decreased the flip angle of refocusing pulses to 150° from the ideal flip angle of 180° in order to remain within the accepted SAR range [14], although this might reduce image quality due to a decreased signal gain and change in contrast [16]. Also, in the study of SPACE-using MRC by Haystead et al., adopted parameters were: voxel size (before interpolation processing), 1.25 mm × 1.17 mm × 1.3 mm; 72 slices with an interpolated section of 1 mm [17]. This is 106% larger in voxel size and 3% smaller in coverage volume compared to our study, though smaller in voxel size compared to their constant flip angle sequence. In contrast to these previous studies, we realized high-resolution MRC with excellent image quality using the SPACE technique. The use of the SPACE sequence, which gathers high signal intensities only for the echoes used to acquire the low phase-encoding steps, allows a significant reduction in the SAR, while maintaining the SNR [15,16]. As discussed in our previous work, the SPACE technique should be employed for 3D MRC to make use of the advantage of 3 T, especially when a high spatial resolution and high volume coverage are adopted [18].

On the other hand, there was no significant difference in the visibility of cystic duct insertion between 3 and 1.5 T, although the score was higher with 3 T. This result is consistent with previous studies in which 3D MRC at 3 T provided a slightly better visibility of the cystic duct or cystic duct insertion compared to 1.5 T [7,14]. We speculate that the artifact of gas and/or peristalsis from the duodenum occasionally reduces image quality at the site of cystic duct insertion. Susceptibility artifacts are said to increase at a higher magnetic strength, which might be another drawback of 3 T on MRC imaging [11,12]. However, this is not a major hurdle in applying the 3 T MR system to MRC imaging, because the visibility of the cystic duct was slightly better with 3 T compared to 1.5 T in the studies mentioned above.

The ability to depict non-dilated IHBD may have many clinical applications, including the diagnosis of small hepatolithiasis, primary sclerosing cholangitis, or the preoperative assessment of the biliary system in living-related liver donors. Some authors reported that MRC obtained with conventional 2D methods at 1.5 T has the capability to assess non-dilated biliary anatomy in potential donors but is insufficient in terms of accuracy [6,9,10]. Also, other reports have indicated that iodipamide meglumine-enhanced multidetector row CT (MDCT) cholangiography is superior to MRC (including conventional 2D T2-weighted MRC and mangafodipir trisodium-enhanced excretory MRC) for the preoperative assessment of the biliary tract [21,22], although adverse reactions to CT biliary contrast agents are reportedly observed in 1–3% of subjects [21,23]. On 3D MRC with SPACE at 3 T in our study, the mean score of the third branches of the IHBD were 3.9, and the fourth or more peripheral branches of the IHBD were detectable in 13 of 17 volunteers. Schroeder et al. reported that the third or fourth branches of the IHBD were frequently visualized clearly on MDCT cholangiography [22,23], and our result is comparable to this. 3D MRC with the SPACE technique at 3 T can generate sufficient information on the anatomy of the non-dilated IHBD during the preoperative assessment of potential donors, without the risk of reactions to contrast agents or ionizing radiation exposure.

There were certain limitations in our study. First, only a small number of subjects were assessed to evaluate MRC imaging. Our results should be validated through further studies. Secondly, all MRC images in our study were obtained under free-breathing using the respiratory triggering technique (PACE). A few subjects showed respiratory misregistration even with the PACE technique. Therefore, it might be necessary in clinical examinations to conduct breath-hold MRC (breath-hold thick-slab 2D TSE and/or breath-hold multislice HASTE) in combination with free-breathing navigator-triggered MRC. Thirdly, our study population was healthy, so we do not have data on biliary disorders. Therefore, the clinical utility of 3D MRC with SPACE at 3 T in evaluating pathological states needs to be examined in a patient-based study. Fourthly, phased-array coils used were eight-channel at 3 T and six-channel at 1.5 T. Because phased-array coils with more elements may by themselves increase the SNR compared to coils with less elements, this difference might exaggerate the advantage of 3 T.

5. Conclusions

3 T MRC using SPACE offered better image quality compared to 1.5 T MRC with SPACE, especially in the visualization of the